FIBER OPTIC CURRENT SENSOR INTERROGATED BY PHASE-SENSITIVE OPTICAL TIME-DOMAIN REFLECTOMETER

A Thesis Submitted to
the Graduate School of Engineering and Sciences of
İzmir Institute of Technology
in Partial Fulfillment of the Requirements for the Degree of

MASTER OF SCIENCE

in Electronics and Communication Engineering

by
Şamil Şirin

July 2022
İZMİR

ACKNOWLEDGMENTS

Firstly, I would like to thank my supervisor Dr. Kıvılcım YÜKSEL ALDOĞAN for her continuous support since my undergraduate years and for giving me the chance of working with her Ph.D. supervisor Prof. Dr. Marc WUILPART, to whom I am deeply indebted for his help that saved me from being stuck in troublesome mathematical expressions of the polarization concept.

I would like to extend my sincere thanks to my family, namely my father for his encouragement to begin my master's degree program while most of my peers immediately took the job opportunities in the industry; my mother for her guidance to me in the hardest times; my sister for her motivational speeches; and my grandmothers for their spiritual support.

I also owe a debt of gratitude to my dear aunt Ayten ZEYTİNOĞLU, her spouse Bülent, and their children Aslı and Emre for becoming my family in İzmir. They have always made me feel at home since the beginning of my bachelor's degree in 2014.

Lastly, many thanks to my colleagues (research assistants) and friends who were with me during my graduate studies.

ABSTRACT

FIBER OPTIC CURRENT SENSOR INTERROGATED BY PHASE-SENSITIVE OPTICAL TIME-DOMAIN REFLECTOMETER

In this thesis, a novel method for current sensing using an FBG-assisted Phase-Sensitive Optical Time Domain Reflectomter (Phase-OTDR) with Mach-Zehnder Interferometer is proposed. The detrimental effect of the intrinsic linear birefringence of the sensing fiber is solved by calibration. An FBG pair is written at the two ends of the spun fiber coil to eliminate phase fading and increase the measurement accuracy. A simulation tool was developed to study the feasibility of the approach and the sensor performance by a well-established Phase-OTDR model with the Jones formalism. The effects of bending- and FBG-induced linear birefringence are investigated as well as the impact of the detector noise.

ÖZET

FAZA-DUYARLI ZAMAN BÖLGESİNDE OPTİK GERİ YANSITICI İLE SORGULANAN FİBER OPTİK AKIM SENSÖRÜ

Bu tezde, Faza-Duyarlı Zaman Bölgesinde Optik Geri Yansıtıcı (Faz-OTDR) ile akım ölçümü için Mach-Zehnder İnterferometreli, Fiber Bragg Izgara-Destekli yeni bir metod önerilmiştir. Algılayıcı fiberin kendi iç doğrusal çiftkırınımının olumsuz etkisi kalibrasyonla giderilmiştir. Faz sönümlenmesini ortadan kaldırmak ve ölçüm doğruluğunu arttırmak için spun fiberden oluşan sarımın başına ve sonuna bir çift fiber Bragg ızgara (FBG) yazılmıştır. Yaklaşımın fizibilitesi ile sensör performansını çalışabilmek amacıyla iyi bilinen bir Faz-OTDR modeli ve Jones formalizm kullanılarak bir simülasyon aracı geliştirilmiştir. Bununla, bükülme ve FBG kaynaklı doğrusal çiftkırınımın etkileri ve dedektör gürültüsünün tesiri incelenmiştir.

TABLE OF CONTENTS

LIST OF FIGURES vii

LIST OF TABLES ix

LIST OF ABBREVIATIONS x

CHAPTER 1. INTRODUCTION 1

1.1. Overview of physical principles behind current sensing techniques 1

1.2. Distributed current sensing via backscattering techniques 6

1.3. Motivation of this Thesis 8

CHAPTER 2. THEORETICAL BACKGROUND 10

2.1. Mathematical Description of Polarization 10

2.2. Optical Fiber Polarization Properties 13

2.3. Poincaré Sphere 16

2.4. Optical Time Domain Reflectometry (OTDR) 17

2.4.1. Phase-Sensitive OTDR (φ-OTDR) 18

2.4.2. Mach Zehnder (MZ) supported φ-OTDR 19

2.4.3. FBG-Assisted φ-OTDR 20

CHAPTER 3. PROPOSED DESIGN AND MODELLING 23

3.1. Design Considerations 23

3.2. Jones Analysis of the Proposed Design 25

3.3. Sensor Calibration 27

3.4. Simulator Tool Development 28

3.4.1. Backscattering Model without Polarization Effects 29

3.4.2. Jones Matrix of Optical Fiber 31

3.4.3. Revised Backscattering Model with Polarization Effects 32

3.4.4. Adding FBG to the Model 34

CHAPTER 4. RESULTS AND DISCUSSION 36
4.1. Tracing the SOP via Poincaré Sphere 36
4.2. φ-OTDR Simulation Results..... 39
4.3. FBG-Assisted φ-OTDR Simulation Results 42
4.4. Orientation of FBG and Coil Bending 45
4.5. Detector Noise Effect 45

CHAPTER 5. CONCLUSION 49

REFERENCES 50

LIST OF FIGURES

Figure **Page**

Figure 1.1. Basic polarimetric FOCS configuration 3
Figure 1.2. Modified polarimetric FOCS, also known as dual-quadrature scheme ... 5
Figure 1.3. Reciprocal reflection interferometer 6
Figure 1.4. Reflectometric-based interrogation techniques 7
Figure 1.5. Physical principles of current sensors 8
Figure 2.1. Polarization states: Arrows denote the sense of rotation 11
Figure 2.2. Illustration of a general ellipse and its parameters 13
Figure 2.3. Several SOPs are represented as dots on the Poincaré sphere. 16
Figure 2.4. OTDR schematic 17
Figure 2.5. 3D demonstration of φ-OTDR power trace (Hartog, 2017) 19
Figure 2.6. MZ configuration for detection part of φ-OTDR. 20
Figure 2.7. Demodulated phase after MZ interferometer 20
Figure 2.8. FBG-Assisted φ-OTDR power trace where UWFBG is at 10th meter. ... 22
Figure 2.9. Interference of FBG reflections 22
Figure 3.1. Proposed current sensing system 25
Figure 3.2. Pulse and fiber models. Pulse is assumed to be moving rightward. 29
Figure 3.3. Scattering interval models 35
Figure 4.1. Change of SOP as light propagates forward and backscatters. 36
Figure 4.2. SOP evolution along the proposed fiber line 37
Figure 4.3. SOP evolution along the proposed fiber line 39
Figure 4.4. Sensing setup without FBGs. 40
Figure 4.5. Rayleigh backscattering power detected by the three detectors. 40
Figure 4.6. Demodulated phase trace. 41
Figure 4.7. Sensing setup when FBGs are included. 42
Figure 4.8. Backscattered and reflected signal power received by the 3 detectors. ... 43
Figure 4.9. Demodulated phase trace when FBGs are included. 43
Figure 4.10. Linear approximation to the scale factors 45
Figure 4.11. Effect of FBG orientations on the scale factor 46

Figure **Page**

Figure 4.12. Effect of bending orientation on the scale factor 46

Figure 4.13. Error bar for the demodulated phase 47

Figure 4.14. Percentage error obtained for currents from 200 A to 40 kA 48

LIST OF TABLES

Table **Page**

Table 4.1. Fiber parameters 37

Table 4.2. Comparison of expected and demodulated phase 41

Table 4.3. Expected and demodulated phase when FBGs are included 44

LIST OF ABBREVIATIONS

DC . . . . . Direct Current
AC . . . . . Alternative Current
CT . . . . . Current Transformer
RC . . . . . Rogowski Coil
TGG . . . . . Terbium Gallium Garnet
FOCS . . . . . Fiber Optic Current Sensors
LCP . . . . . Left Circularly Polarized
RCP . . . . . Right Circularly Polarized
LEP . . . . . Left Elliptically Polarized
REP . . . . . Right Elliptically Polarized
LP . . . . . Linearly Polarized
MI . . . . . Modulation Instability
QWP . . . . . Quarter Wave Plate
FBG . . . . . Fiber Bragg Gratings
ABB . . . . . ASEA Brown Boveri
DOFS . . . . . Distributed Optical Fiber Sensors
OTDR . . . . . Optical Time Domain Reflectometry
φ-OTDR . . . . . Phase-Sensitive OTDR
POTDR . . . . . Polarization-Sensitive OTDR
BOTDR . . . . . Brillouin OTDR
ROTDR . . . . . Raman OTDR
ITER . . . . . International Thermonuclear Experimental Reactor
PMF . . . . . Polarization Maintaining Fiber
SSMF . . . . . Standard Single-Mode Fiber
PMC . . . . . Polarization Mode Coupling
SOP . . . . . State of Polarization
UWFBG . . . . . Ultra Weak FBG
inf . . . . . infinite

CHAPTER 1

INTRODUCTION

There are numerous techniques to measure electrical current that have been evolved for decades. Among them, optical current sensors draw a particular interest due to their small size, lightweight, and good insulating ability. Therefore, a particular focus will be placed on the optical current sensing techniques in this part.

1.1. Overview of physical principles behind current sensing techniques

Ohm's Law is the most known current measurement method. A simple shunt resistor can provide a resolution of 10s of μA and be used to detect currents up to a few amperes. It has low cost, small size, linear and fast response, but its power dissipation grows with the square of current amplitude which may result in excessive heat generation. Besides, it must interfere the circuit of the current by direct contact, leading unexpected circuit response, if the circuit design cannot handle the sensor resistance and the potential parasitic effects (Ramsden, 2006a).

The principles other than Ohm's Law are based on sensing the magnetic field around the current avoiding direct contact with the conductor [1]. One of them is the Hall effect which exploits the Lorentz force generated by the magnetic field on a thin metal strip. It produces a potential difference between two sides of the strip proportional to the magnetic field strength (Ramsden, 2006a). The performance of Hall effect-based sensors is mostly determined by the complexity of the transducer circuit. Simpler circuits provide lower cost as well as less power consumption but suffer from poor linearity and slow response. As the complexity increases, response time and linearity get better, while the sensing range is narrowed. This type of sensor is mostly used for direct current (DC)

[1] Ampere's Law states that current flowing through a wire creates a magnetic field around itself so that the line integral of the field strength around a path enclosing the current gives the current magnitude.

measurement.

For alternating current (AC) measurement, Current Transformer (CT) and Rogowski Coil (RC) are well-established transducers that are often used to monitor high currents. Both rely on Faraday' s law of induction which states that varying magnetic flux enclosed by a path generates an electromotive force around that path (Ramsden, 2006b). CT differs from RC by having a magnetic core. It provides better sensitivity but also brings higher cost and possibility of saturation or magnetic hysteresis. (Samimi et al., 2015).

There are also studies on alternative methods based on magnetostriction and magnetoresistance. The materials owning these properties experience shape (magnetostriction) or resistance change (magnetoresistance) as a response to magnetic field. Thus, those changes can be measured and be related to the field intensity. This kind of materials commonly suffers from hysteresis (Cubells-Beltran et al., 2011) which can be reduced by magnetically or electrically biasing magneto-resistive element (Vopálenský et al., 2004), and applying physical pressure on the magneto-strictive material (Satpathi et al., 2005). Both the methods can measure direct or alternating currents below 1 kA (Cremonezi et al., 2013; Slatter et al., 2019), but magneto-strictive ones cannot go beyond kHz range (Lopez et al., 2019; Zhang et al., 2012) while there are reported magneto-resistive-based configurations that can sense up to 1 GHz (Slatter et al., 2019). Magneto-resistive elements are interrogated by an external electrical circuit, while magneto-strictive sensors can be interrogated by fiber-optic based passive strain sensors (Lopez et al., 2019; Masoudi and Newson, 2014).

Besides the methods mentioned above, there are optical current sensors that exploit magneto-optic materials. Their underlying principle is known as Faraday effect which states that if a magneto-optic material is under magnetic field, it rotates the linear polarization axes of propagating light in the element by an angle that is proportional to the magnitude of magnetic field parallel to the light direction. The proportionality factor is described by a wavelength dependent constant called "Verdet constant" (Saleh and Teich, 2007). It depends on the magneto-optic characteristic of the material and is desired to be high for a measurable response to magnetic field. Crystals of terbium gallium garnet (TGG) are widely preferred Faraday rotators due to their high Verdet constants (Kumari and Chakraborty, 2018). However, to detect the amount of Faraday rotation correctly,

polarization of light must be kept unperturbed until detection, which is difficult if the transmission medium (e.g., optical fiber) is birefringent. Bulk-glass optical sensors are less affected by the birefringence since they guide light through free-space (Ning et al., 1995). Nonetheless, they require stringent conditions to provide critical-angle reflection at each reflecting surface (Woolsey et al., 1997). Additionally, they cannot be mounted and maintained as practically as fiber optic-based sensors. With the development of fiber manufacturing techniques and fiber-compatible components, promising solutions to overcome the detrimental effects of the fiber birefringence are discovered. Thus, a vast majority of the published studies on optical current sensors have employed optical fibers as guiding medium for the last decade.

Optical fiber itself is a magneto-optic material, so it can be used as the sensing element besides the transmission purpose, enabling "all-fiber" configurations. Although its main constituent, fused silica has a relatively low Verdet constant, it can be coiled around the current carrying conductor so that the light experiences Faraday effect for much longer distances. Alternatively, doping the fiber with rare earth atoms such as terbium and europium enhances Verdet constant, however, for many configurations, the trade-off between the sensitivity and the maximum measurable current must be considered such that the maximum Faraday rotation must be small (less than 2π) to maintain linearity (Huang et al., 2015, 2016).

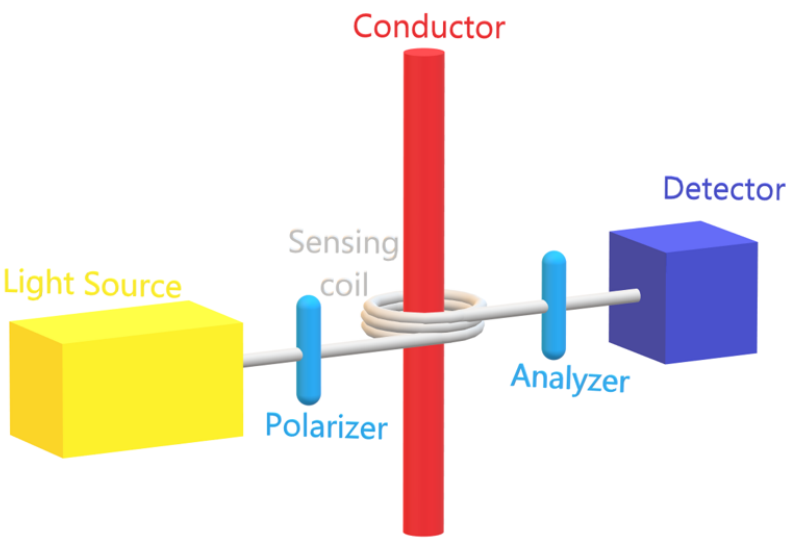

Figure 1.1. Basic polarimetric FOCS configuration

Fiber optic current sensors (FOCS) detect Faraday rotation angle via polarimetric or interferometric interrogation (Donati et al., 1988). Basic polarimetric FOCS setup is composed of a polarizer and an analyzer (polarizer behind the detector) besides the light source, detector, and optical fiber as seen in the Figure 1.1 (Papp and Harms, 1980). Linearly polarized input light goes under a Faraday rotation when passing through the sensing fiber coil. Then, it passes through the analyzer which yields a sinusoidal optical power at the output. However, polarization-independent power fluctuations of incoming light due to losses or source itself would corrupt the resulting rotation angle. Thus, it is better to use relative amplitudes of the polarization components. That can be achieved by employing two or more analyzers with known relative orientations following a beam splitter as shown in Figure 1.2. Note that, as the system complexity increases, hardware imperfections due to imprecisely aligned polarizers (analyzers), unequal splitter ratio, etc. can cause deviations from ideal sensor response. A straightforward post-processing algorithm is presented in (White et al., 2010) to reduce such deviations. Another source of error in FOCS is linear birefringence that can be present in both the transmitting and sensing optical fibers. As a solution, Faraday mirror which reflects light with a 90° orthogonal polarization relative to the input SOP, is placed at the end of sensing coil, so in the return path of reflected light, the amount of rotation is doubled thanks to the non-reciprocal nature of Faraday effect while the influence of linear birefringence reduces. Even though, this method provides an improvement, it cannot totally compensate the effect of the birefringence in the presence of magnetic field (Gao and Zhao, 2019; Jiao et al., 2006; Alasia and Thévenaz, 2004; Karabulut et al., 2019; Leysen et al., 2019).

Faraday rotation occurs due to magnetic field-induced circular birefringence of the sensing element. Thus, when left circularly polarized (LCP) and right circularly polarized (RCP) waves are sent through fiber simultaneously, they experience different refractive indices. Consequently, it causes a phase difference proportional to the Faraday rotation angle which can be detected through interferometric FOCS. In interferometric approach, linear birefringence is compensated by using either twisted or spun fiber for sensing coil (see Section 2.2 for details). Kersey and Jackson (Kersey and Jackson, 1986) proposed frequency modulated heterodyne detection with Michelson interferometer. Despite the technology of that time which did not allow an effective compensation of phase noise, the measured noise was found to be 3 mA/$\sqrt{}$Hz, providing a sensing

range up to 100 A. Two years later, Nicati and Robert (Nicati and Robert, 1988) proposed Sagnac-interferometer with additional intensity measurement before the interference to solve the stability problem due to fiber birefringence and variations in the intensity of the injected signal. In 1994, Frosio and Dandliker in cooperation with ABB (Frosio and Dändliker, 1994) proposed "reciprocal reflection interferometer" with the combination of high birefringent (hi-bi) fiber, sensing coil (twisted or spun fiber), a quarter-wave plate (QWP), all-fiber piezoelectric birefringent phase modulator, and a mirror as seen in Figure 1.3. In the same year, almost same configuration was developed independently at Texas A&M University (Blake et al., 1994). Both configurations employed a low-coherence source providing good signal stability despite the non-ideal retarders and varying temperature. In the following years Bohnert, et al. in corporation with ABB (Bohnert et al., 2002) improved the reciprocal reflection interferometer so that obtaining high immunity to vibrations with frequencies up to 500 Hz and 10g of acceleration as well as to temperature variation between -40 to 80 degrees. The sensor also offered measurements up to 500 kA with a percentage error less than 0.1% (Bohnert et al., 2007).

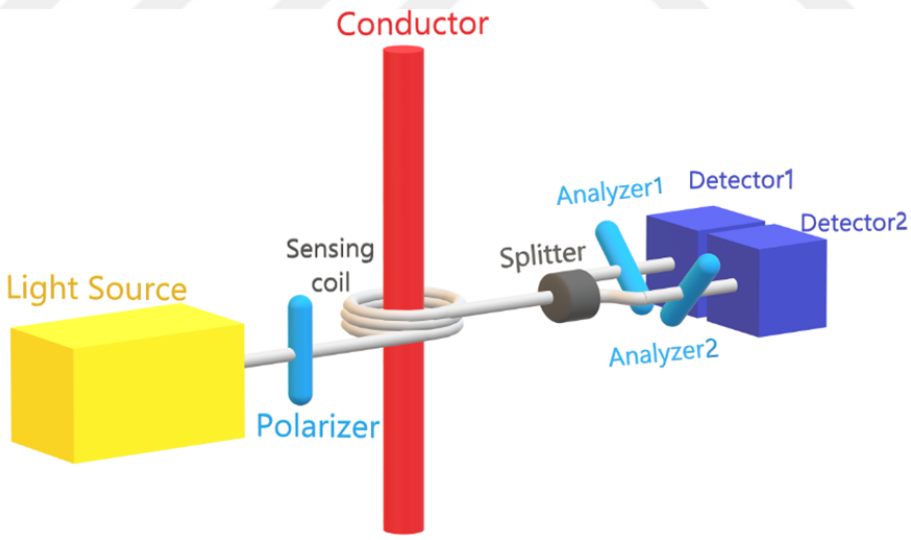

Figure 1.2. Modified polarimetric FOCS, also known as dual-quadrature scheme: It employs two analyzers and two detectors. Faraday rotation would be proportional to the difference-sum ratio of detected intensities, which is independent of initial power of light source.

In addition to the approaches referred above, there are studies on magneto-optic properties of fiber-Bragg grating (FBG) for magnetic field sensing purpose (Wu et al., 2013; Caucheteur et al., 2017; Peng et al., 2012; Orr and Niewczas, 2011; Caucheteur et al., 2006). Yet, except the systems combined with magnetic fluids (Zheng et al., 2013; Zhang et al., 2016), the number of experiments in this approach is insufficient and they have relatively poor resolution compared with the sensing range.

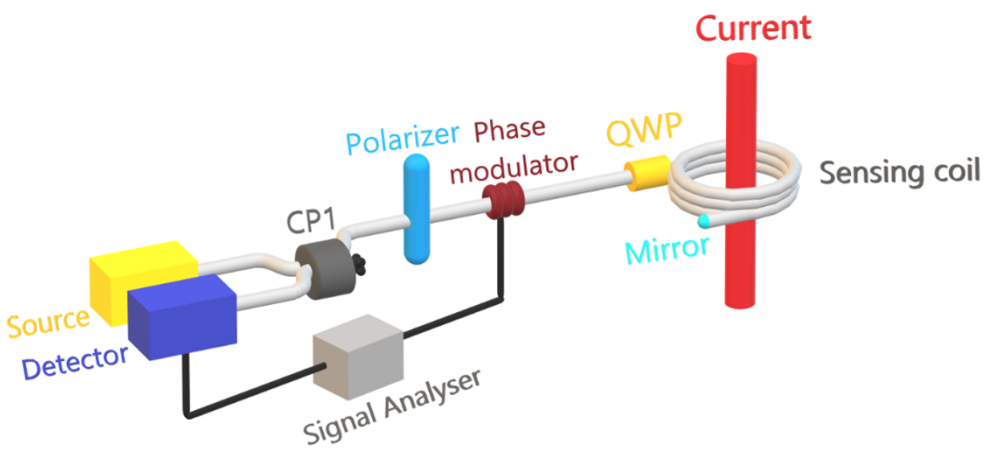

Figure 1.3. Reciprocal reflection interferometer proposed by (Frosio and Dändliker, 1994)

1.2. Distributed current sensing via backscattering techniques

The configurations mentioned in the previous section allow for detection of total Faraday rotation. On the other hand, "all-fiber" systems have the advantage of distributed or quasi-distributed sensing via backscattering techniques. They allow monitoring Faraday rotation along the sensing fiber. Distributed sensing technologies exploit Rayleigh, Brillouin, or Raman scattering. In Brillouin and Raman scattering, there is an interaction of light waves with large scale acoustic phonons and vibrational/rotational modes of molecules, respectively, which results in scattered waves with shifted frequencies (Muanenda et al., 2019). On the other hand, Rayleigh scattering is an elastic process caused by silica molecules. Distributed Optical Fiber Sensors (DOFS) detect the back-guided

portion of the scattered signal, referred to as "backscatter", as a function of time or frequency. The backscattered signal carries information about power loss, refractive index variation or optical path length change occurred somewhere along the path of the backscattered signal, by means of its certain properties such as intensity, polarization, phase, and frequency as shown in Figure 1.4.

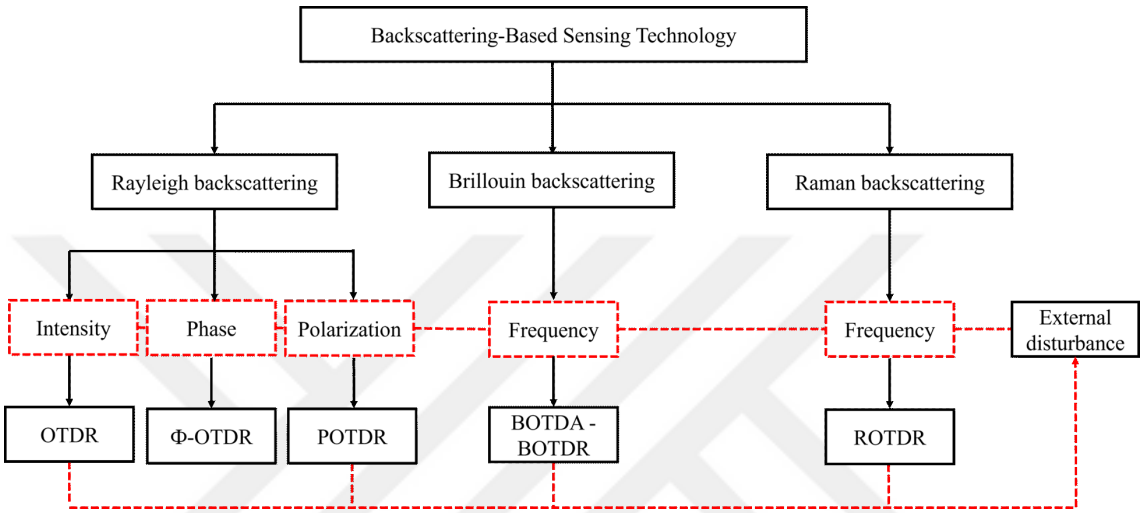

Figure 1.4. Reflectometric-based interrogation techniques: Optical Time Domain Reflectometry (OTDR), Phase-Sensitive OTDR (φ-OTDR), Polarization-Sensitive OTDR (POTDR), Brillouin Optical Time Domain Analysis (BOTDA), Brillouin OTDR (BOTDR) and Raman OTDR (ROTDR).

Besides the environmental sensing applications, backscattering techniques are also employed for fiber characterization including the determination of polarization mode dispersion, attenuation, etc. Wuilpart, et al. (Wuilpart et al., 2000) proposed Polarization-Sensitive Optical Time Domain Reflectometry (POTDR) for distributed measurement of fiber birefringence and noted the potential application of this technique for magnetic field sensing. In the last decade, the mathematical model for POTDR-based ultra-high current sensing (up to orders of mega-amperes) was established and the feasibility of using it for International Thermonuclear Experimental Reactor (ITER) fusion reactor was studied (Wuilpart et al., 2011; Aerssens et al., 2012; Motuz et al., 2019). The performance of the technique was experimentally validated on the Tore Supra fusion reactor (Wuilpart et al., 2017, 2018).

Distributed current sensing by POTDR does not rely on small angle approximation as in the most polarimetric and interferometric configurations. It permits monitoring how much rotation accumulates gradually as a function of distance z. Thus, total Faraday rotation can even be greater than 2π provided that the spatial resolution is high enough. Therefore, it is a promising approach for high-current measurements as an alternative to Rogowski coil (Aerssens et al., 2012).

As a summary, physical principles are given together in the Figure 1.5.

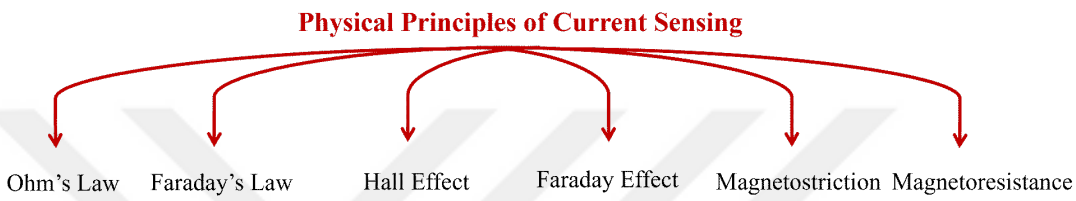

Figure 1.5. Physical principles of current sensors

1.3. Motivation of this Thesis

Recently, distributed sensing based on Phase-Sensitive OTDR (φ-OTDR) has become a trending research area as well as a commercialized technique. It is mostly used for monitoring acoustic signals that causes a strain change on the optical fiber. Nonetheless, it is not limited to strain sensing since any perturbation that induces a variation in the refractive index or in the optical path length causes phase change in the backscattered signal. For example, in 2015, φ-OTDR was proposed for distributed birefringence measurement, but the proposed system was not capable of discriminating linear and circular birefringence (Soto et al., 2015). In 2021, φ-OTDR with pulse compression was presented for linear birefringence measurement (Chen et al., 2021).

Current measurement based on Faraday effect is nothing but circular birefringence measurement in a dynamic manner, so φ-OTDR can be a promising candidate for distributed current sensing when designed with proper optical polarization components. It would have all the advantages that a FOCS has such as light-weight, small size, and robustness. Besides, it can provide distributed sensing so that multiple current carrying

conductors can be monitored by a single fiber line at the same time.

The aim of this Thesis is to evaluate the feasibility of φ-OTDR-based current sensing via simulations on MATLAB. The Thesis is organized as follows: Chapter 2 covers the fundamentals of polarization in optical fiber, fiber Bragg gratings, and the working principles of POTDR and φ-OTDR techniques. In Chapter 3, development of the φ-OTDR simulator tool based on modular programming is described in detail. In Chapter 4, obtained results from the simulator are presented and discussed. Lastly, in Chapter 5, the work in the Thesis is summed up and projections are stated.

CHAPTER 2

THEORETICAL BACKGROUND

This chapter explains the basics of polarization in optical fibers, fiber Bragg grating (FBG) sensors, and principles of optical time-domain reflectometry techniques to provide an adequate technical background required to follow the work presented in this Thesis.

2.1. Mathematical Description of Polarization

A monochromatic light wave traveling in an optical fiber can be described by its associated electric field vector perpendicular to the propagation direction (in a homogeneous medium and under the weakly guiding approximation (Saleh and Teich, 1991)). If the wave propagates along the z direction of a Cartesian coordinate system, the electric field lies on the x-y plane (polarization plane). In general, it is described by

$$\vec{E}\left(t,\ z\right) = \Re\left\{\left[E_x\hat{\mathbf{x}} + E_y\hat{\mathbf{y}}\right]\exp\left[j2\pi f\left(t - \frac{z}{c}\right)\right]\right\} \tag{2.1}$$

where E_x and E_y are complex amplitudes, f is the optical frequency, c is speed of light in vacuum and $\hat{\mathbf{x}}$ and $\hat{\mathbf{y}}$ are unit vectors along x and y directions. As time t starts from an arbitrary point t_0, and increases until $t = t_0 + 1/f$, tip of the vector $\vec{E}\left(t\right)$ draws either a line, an ellipse, or a circle on the polarization plane as seen in Figure 2.1. Then, state of polarization (SOP) of the light wave is said to be either 'linear', 'elliptical' or 'circular', accordingly.Then, state of polarization (SOP) of the light wave is said to be either 'linear', 'elliptical' or 'circular', accordingly.

Since both the x and y components have common complex exponential time-dependent term, E_x and E_y are sufficient to describe a SOP. Thus, omitting the complex exponential, Equation 2.1 can be written in a 2-dimensional vector form:

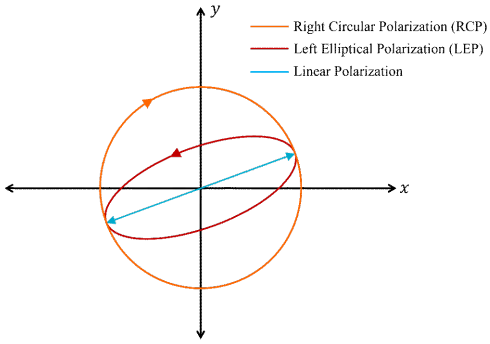

Figure 2.1. Polarization states: Arrows denote the sense of rotation

$$\vec{\mathbf{E}} = \begin{bmatrix} E_x \\ E_y \end{bmatrix} \tag{2.2}$$

which is known as Jones vector. Here, relative phases and amplitudes of E_x and E_y define a unique SOP. Therefore, Jones vector can be normalized by the total power $|E_x|^2 + |E_y|^2$. For further simplicity, normalized Jones vector also can be scaled by the phase of x component $\arg\{E_x\}$ such that:

$$\frac{\begin{bmatrix} E_x \\ E_y \end{bmatrix}}{\left(|E_x|^2 + |E_y|^2\right) \exp\left[j \arg\{E_x\}\right]} = \begin{bmatrix} a_x \\ a_y \angle \Delta\phi \end{bmatrix} \tag{2.3}$$

where $a_x = \frac{|E_x|}{|E_x|^2 + |E_y|^2}$, $a_y = \frac{|E_y|}{|E_x|^2 + |E_y|^2}$ and $\Delta\varphi = \arg\{E_y\} - \arg\{E_x\}$.

Sign of the phase difference $\Delta\varphi$ indicates the sense of rotation for an observer who looks toward the approaching beam [1]. If it is positive (negative), the tip of the electric field rotates clockwise (counter-clockwise) along the ellipse, which is called right-elliptical polarization (left-elliptical polarization) and abbreviated as REP (LEP).

Linear and circular SOPs are indeed special cases of elliptical SOP, so the following parameters defining a general ellipse are needed to be related to the three terms, a_x,

[1] Physicists define the sense of rotation according to right hand rule, so they assume the observer looks towards the leaving beam, which is the opposite of the accepted convention by engineers.

a_y and $\Delta\varphi$, in the normalized Jones vector in Equation 2.3:

- the ellipticity e; defined as the ratio of the semi-minor axis (denoted by b) to the semi-major axis (denoted by a) with a positive or negative sign depending on the sense of rotation.
- the azimuth θ; defined as the angle between the major axis of the ellipse and the x-axis.

Two additional parameters α and χ are needed to be defined as follows:

$$\alpha = \tan^{-1}(a_y/a_x) \tag{2.4}$$

$$\tan(\chi) = e = \pm b/a \tag{2.5}$$

The parameter χ is defined in the range of $[-\frac{\pi}{4}, \frac{\pi}{4}]$, so the ellipticity is defined between -1 and 1. The parameter α relates χ to $\Delta\varphi$ by the following equation so that it can be used to find the ellipticity e by Equation (2.5):

$$sin(2\chi) = \sin(2\alpha)\sin(\Delta\varphi) \tag{2.6}$$

The azimuth θ is related to $\Delta\varphi$ via α again, as in the following equation:

$$\tan(2\theta) = \tan(2\alpha)\cos(\Delta\varphi) \tag{2.7}$$

The mentioned ellipse parameters are illustrated in 2.2.

Elliptical SOP can converge to linear or circular SOP. In the former case, the ellipticity approaches zero. This leads the tip of electric field vector to move on a straight line. It happens when either $\Delta\varphi$ is equal to any integer multiples of π or α becomes zero

by setting one of a_x or a_y to zero. In the latter one, the ellipticity is 1 or -1 and $\Delta\varphi$ is an odd multiple of $\frac{\pi}{2}$. That forces α to be an odd multiple of $\frac{\pi}{4}$ which consequently results in $a_x = \pm a_y$. Eventually, the field tip follows a circular path. Such a light is said to be right-circularly polarized (RCP) or left-circularly polarized (LCP) depending on the sign of ellipticity.

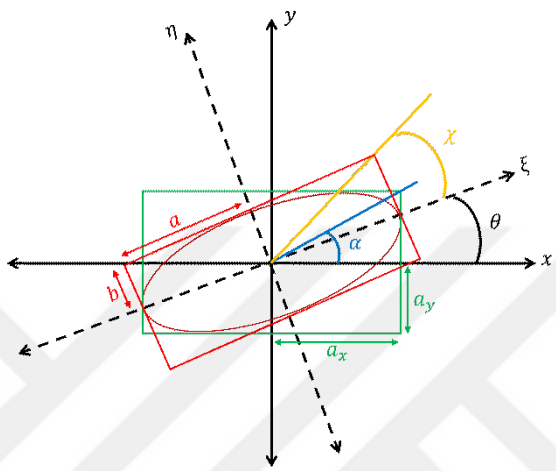

Figure 2.2. Illustration of a general ellipse and its parameters

In real life, monochromatic light does not exist, in other words, a light wave must have a non-zero optical bandwidth (linewidth). Thus, overall electric field is a combination of many fields associated with the corresponding frequencies in the spectrum. If their directions are totally irregular, intensity of linear polarized components would be equal in all directions, even if the light is passed through an arbitrary retarder with an arbitrary azimuth (Prakash and Chandra, 1971). In this case, overall polarization is unpredictable, and the light is said to be "unpolarized", as in the example of sunlight. In general, however, polarization is neither completely deterministic nor totally random. In other words, it is "partially polarized" as in the case of light emitted by a narrow-band (quasi-monochromatic) laser source (Born and Wolf, 1999). For the optical system demonstrated in this Thesis, probe pulse is modelled as totally polarized monochromatic wave since the lasers with almost single frequency (sub-kHz linewidth) are available on the market.

2.2. Optical Fiber Polarization Properties

When light enters a single-mode optical fiber, it splits into two orthogonally polarized modes (eigenmodes) with propagation constants β_1 and β_2. Ideally, the constants are equal so that both the modes experience same refractive index and called degenerate modes. In practice, however, they slightly differ from each other due to imperfect circular shape of the fiber core cross section, non-uniform stress distribution on the core and inhomogeneous dopant concentration. As the orthogonal modes propagate down the fiber, their phases change differently due to unequal propagation constants. After one meter of propagation length, their phase difference changes by an amount of $\beta_2 - \beta_1$, which is defined as birefringence. The phase difference changes by 2π after a certain propagation length, called beat length (L_B) and defined as:

$$L_B = \frac{2\pi}{\beta_2 - \beta_1} \tag{2.8}$$

If the eigenmodes are linearly polarized, the fiber is said to exhibit "linear birefringence". In some fibers, polarization eigenmodes would be circularly orthogonal (one is RCP and the other is LCP) causing circular birefringence, which originates from twist-induced photo-elastic effect and the Faraday effect that occurs in the presence of a magnetic field parallel to the propagation direction. In general, both linear and circular birefringence, can exist together, leading to elliptical birefringence.

In standard single mode fibers (SSMF), birefringence distribution is not uniform due to the imperfections coming from the manufacturing process like varying core-shape and stress distribution along the fiber. Also, the external perturbation like bends, twists, pressure and change of temperature affect the birefringence distribution in a random manner. Consequently, eigenmodes alter through the fiber causing energy transfer between modes, which is called polarization mode coupling (PMC). For how much length the eigenmodes remain unaltered is represented by coupling length (L_C) which varies between 5 and 500 meters for SSMF.

In polarization applications, fibers are usually expected to maintain input SOP along the fiber, but PMC prevents it even if the initial SOP is aligned with one of the

eigenmodes. Thus, Polarization Maintaining Fiber (PMF) is designed to intentionally introduce permanent high linear birefringence (corresponding to a beat length in the few millimeters range) so that the effect of externally induced birefringence becomes comparatively insignificant. Coupling length of PMFs is shown to be in the range of tens of kilometers.

Applications based on Faraday effect relies on determining the magnetic field induced circular birefringence. It requires fiber to have capability of holding circular SOP. However, PMFs can maintain only linear SOP, and they are insensitive to externally induced birefringence originated not only from random perturbation but also from magnetic field. Therefore, low birefringent (low-bi) fibers are more sensitive to Faraday effect. On the other hand, PMC may constitute a serious limitation in low-bi fibers as mentioned above. As a solution, a compromise between PMC and sensitivity can be reached through elliptical birefringent fibers. They rely on rotating the linear polarization axes so that the linear birefringence oscillates between a small negative and positive value (Laming and Payne, 1989). The axes can be rotated by twisting a solidified optical fiber. Twisted fibers have two disadvantages. Firstly, twist rate is restricted by the breakage limit of fiber. As a rule of thumb, it must not exceed 3 twists per meter, which restricts its effectiveness for the linear birefringence compensation (Griffioen and Glaesemann, 2017). Secondly, twists tend to loosen up by time and temperature variation. To avoid these problems, fiber axes can be rotated during the drawing process of fiber which results in what is called a "spun fiber". Spin rate can reach hundreds of radians per meter. Besides, it is more stable in the presence of temperature variation. Also, spinning the fiber before it gets solidified prevents photo-elastic effect-induced circular birefringence. Therefore, spun fibers are commonly used for current-sensing applications.

Transfer matrix for a medium that relates the input Jones vector to the output Jones vector is called Jones matrix. Birefringence properties of a fiber may not be uniform along its whole length, so it can be considered as a concatenation of uniformly birefringent short sections. Jones matrix of kth section with a length of z is given as

$$J_k(z) = \begin{bmatrix} \cos\Delta_k + j\frac{\sin\Delta_k}{\Delta_k}\Re\{B_k\} & \frac{\sin\Delta_k}{\Delta_k}\left[-\Omega_k + j\,\Im\{B_k\}\right] \\ \frac{\sin\Delta_k}{\Delta_k}\left[\Omega_k + j\,\Im\{B_k\}\right] & \cos\Delta_k - j\frac{\sin\Delta_k}{\Delta_k}\Re\{B_k\} \end{bmatrix} \tag{2.9}$$

where $\Delta_k = \sqrt{\Omega_k^2 + B_k B_k^*}$. Ω_k is the effective rotation and B_k is the effective linear retardance (for details, see Section 3.4.2) (Dandu et al., 2022). Then, the overall transfer matrix of whole fiber can be found by the multiplication of those Jones matrices, in the passing order of light through them.

2.3. Poincaré Sphere

Poincaré Sphere is an extremely useful tool to visualize how a SOP evolves along a birefringent medium. Its principles are related to Stokes formalism which is an alternative mathematical description of light polarization. On Poincaré Sphere, any SOP can be represented by a dot as illustrated in Figure 2.3. All the linear SOPs lay on the equator. V and H points are vertically and horizontally aligned linear polarizations, respectively. Right and left circular polarization states correspond to the north and south poles denoted as RC and LC. Elliptical SOPs are in between the poles and the equator.

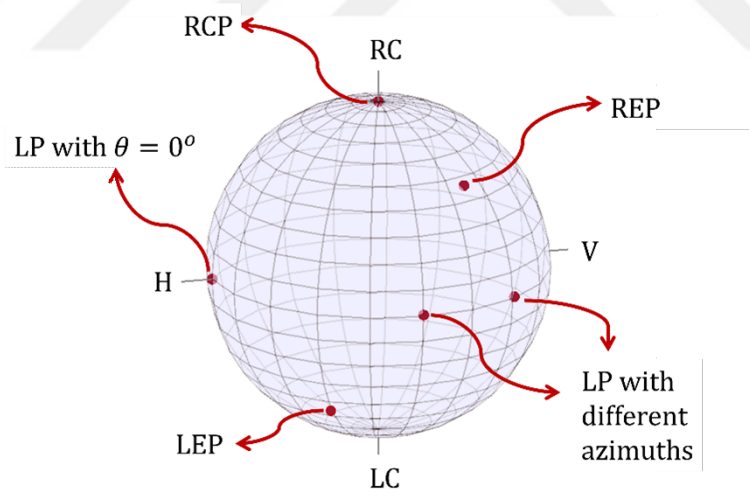

Figure 2.3. Several SOPs are represented as dots on the Poincaré sphere.

A birefringent medium can be defined by its orthogonal eigenmodes. Since the orthogonal SOP pairs are antipodal to each other on Poincaré Sphere, a birefringent medium is represented by an axis called birefringence axis, that is passing through its eigenmodes which are antipodal points. How an initial SOP changes due to birefringence

is determined by simply rotating the initial dot along that birefringence axis on the sphere surface. For example, a SOP that is initially linear (on the equator) remains linear (but with a different azimuth) if it is exposed to a circular birefringence, since the sphere rotates around the RC-LC axis. If the birefringence is 2π, sphere would do a full rotation so that the final SOP will be same with the initial SOP.

2.4. Optical Time Domain Reflectometry (OTDR)

An optical pulse propagating in a single mode fiber continuously experiences Rayleigh scattering due to refractive index fluctuations along the fiber. Optical Time Domain Reflectometry (OTDR) is a measurement technique that measures the power of the back-guided portion of Rayleigh scattering as a function of time. OTDR also refers to the instrument using this technique. Its principle is illustrated in Figure 2.4. The modulator converts continuous light sent by the broadband optical source into an optical pulse with a waveform determined by the signal generator. Circulator guides the pulse to the fiber under test and the backscattered signal to the receiver. Using the information of time delay between the sent pulse and the detected signal, power of the signal backscattered from a particular region of fiber can be identified.

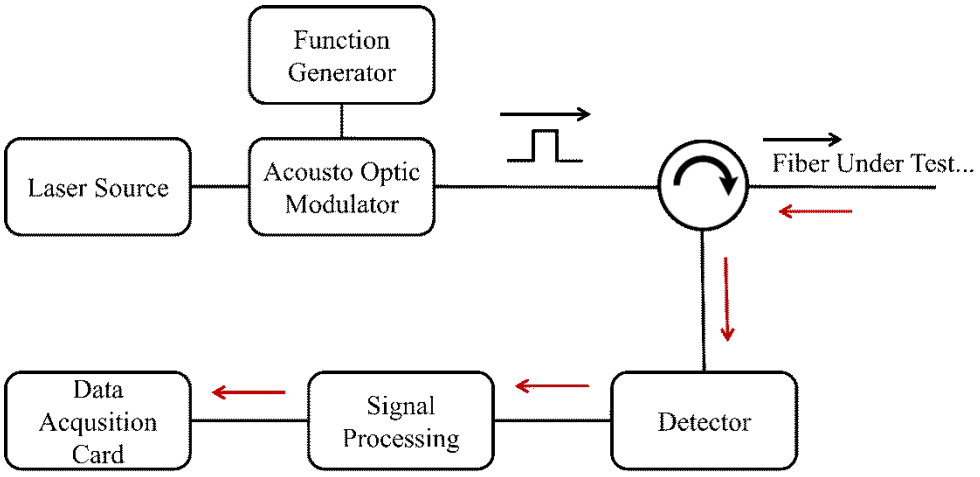

Figure 2.4. OTDR schematic: black arrows represent propagating pulse while red ones do backscattered signal

Signal received by the detector at a time instant is indeed the superposition of many waves backscattered from a section of fiber covered by half of the pulse which is sometimes referred to as "resolution cell". Its length is called "spatial resolution", corresponding to the half the pulse length. If there happens to be two events causing a remarkable power fluctuation in the backscattered signals at two points separated by less than the spatial resolution on the fiber, they cannot be distinguished from each other.

2.4.1. Phase-Sensitive OTDR (φ-OTDR)

Phase of Rayleigh backscattered waves are sensitive to the environmental effects around the fiber. Therefore, phase measurement based on a similar principle to that of OTDR, known as Phase-Sensitive OTDR (or φ-OTDR), is commonly used for various sensing purposes such as vibration, strain, and temperature. Its main difference from conventional OTDR is the narrow linewidth of the optical source so that the coherence length becomes longer than the pulse width. In conventional OTDR, since the coherence length is very short, phases of superposed waves are uncorrelated from each other, causing the overall phase term to vanish at the detector. On the other hand, by virtue of the coherent interference, φ-OTDR keeps phase information of backscattered signals.

φ-OTDR operates by shooting pulses into fiber one after another, with a constant time gap called repetition period, τ_{rep}. The repetition period must be long enough to avoid signals belonging to different pulses to travel in the fiber simultaneously. Power trace obtained from each shot is a function of position (also called "fast time") indicating from which part of the fiber the signal with corresponding intensity scattered back. The traces can be organized along a third dimension in the order of pulse shooting instants, which consequently creates a new axis called "slow time". The resulting graph as seen in Figure 2.5 is useful to follow dynamic variations in both fast and slow time.

Jagged appearance of Rayleigh backscattering power trace comes from the random phase and amplitude of the scattered signals. Yet, that randomness is peculiar to the fiber and remains the same under identical conditions of interrogation (no frequency drift, pulse shape alteration, etc. from trace to trace) and stable environmental conditions (no change in temperature, strain, etc.). When a section of the fiber is subject to a perturbation such as strain, it induces a refractive index variation along the perturbed

region. Thus, light backscattered from anywhere ahead of the perturbed region inevitably experiences a phase change that is proportional to the total refractive index variation. For this reason, the main purpose in φ-OTDR is to extract the differential phase which is the difference of phases belonging to the signals backscattered from before and after the perturbed region. Interferometric φ-OTDR systems such as Mach Zehnder (MZ) supported φ-OTDR inherently obtain the differential phase by physically interfering the backscattered signals coming from consecutive fiber sections. Its details are discussed in the next section.

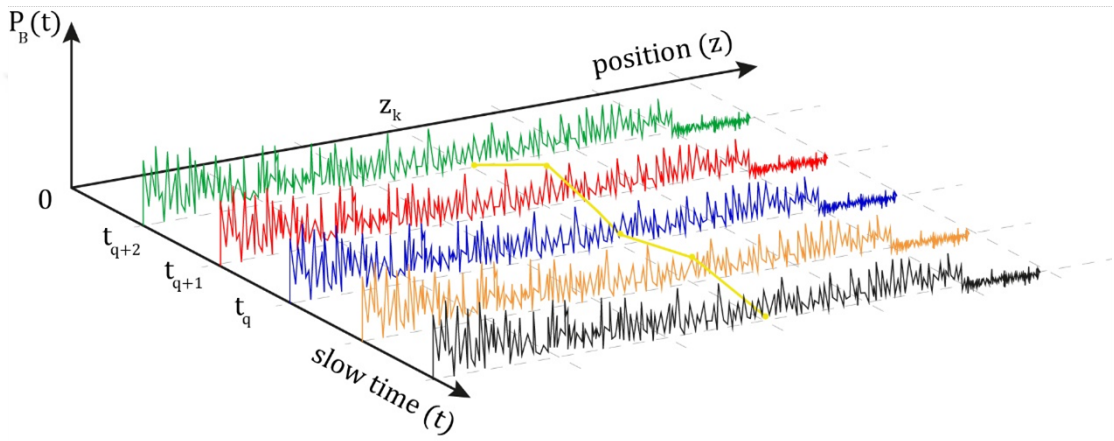

Figure 2.5. 3D demonstration of φ-OTDR power trace (Hartog, 2017)

2.4.2. Mach Zehnder (MZ) supported φ-OTDR

In MZ supported φ-OTDR, signals backscattered from two regions which are denoted in Figure 2.6 as A and B and separated by ΔL, are mixed at the end of the arms that have a length difference of $2\Delta L$. Assuming the light source to be coherent enough (coherence length is longer than the arm length difference of MZ), interference component would be visible in the mixed signal power which is found to be directly related to the phase difference of the backscattered waves from A and B. To extract the phase difference, 3×3 demodulation scheme is employed since it provides more fading elimination than direct manipulation on the mixed signal does (Masoudi et al., 2013). For this reason, MZ interferometer is followed by a 3x3 coupler so that three signals, each

with a $2\pi/3$ radian phase bias are received by three photodetectors. After that, the phase is extracted using a trigonometric identity given in Equation (6) of (Masoudi and Newson, 2017b).

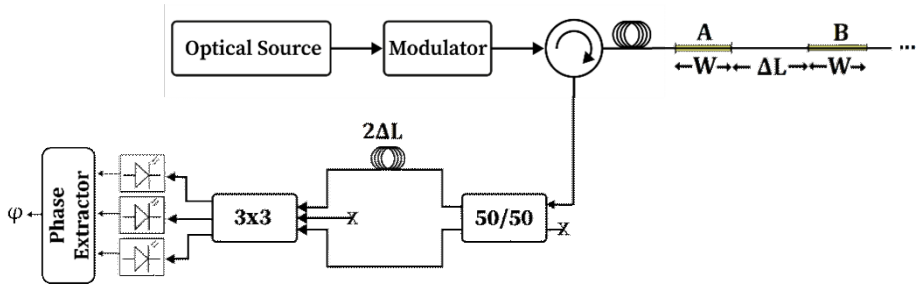

Figure 2.6. MZ configuration for detection part of φ-OTDR.

One of the most critical parameters in MZ configuration is the length of ΔL. To achieve the best performance, it must be longer than the perturbed region length P so that backscatters from sections before and after the perturbation can interfere. On the other hand, longer ΔL causes the appearance of perturbation in the demodulated phase trace to expand and occupy a longer region as shown in Figure 2.7.

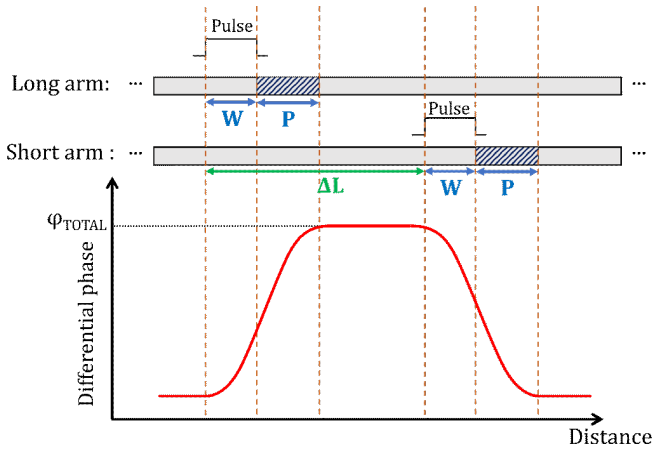

Figure 2.7. Demodulated phase after MZ interferometer: P is the perturbed region length, W is the spatial resolution, φ_{TOTAL} is the total phase change accumulated all along P, and ΔL is the arm length difference of MZ interferometer.

2.4.3. FBG-Assisted φ-OTDR

There are several fading mechanisms occurring in φ-OTDR that degrades the performance: modulation instability (MI), polarization, and interference fading (also known as phase fading). In the scope of this Thesis, the actual limiting factor happens to be interference fading [2]. It arises from destructive interference of Rayleigh backscattered waves at random points, which leads measured signal power to descend so low that the phase extraction becomes erroneous.

Proposed solutions in the literature for interference fading consist of modifications in the interrogator part or in the sensing fiber. The former relies on aggregating multiple measurements taken by pulses in different frequencies, which increases the sensor complexity and restricts the pulse repetition frequency (Hartog, 2017). The latter one suggests enhancing backscattered signal power by ultra-weak fiber-Bragg grating (UWFBG) which is obtained by modifying the refractive index on a small section ($\sim 1mm$ to $\sim 1cm$) of fiber core so that it reflects backwards a portion of a particular wavelength (called Bragg wavelength) of input light (Zhu et al., 2015). Why they are called "ultra-weak" is due to their relatively low reflectivity which lays within a range of -50 dB to -20 dB. Yet, UWFBG reflectivity is still 1 to 5 orders of magnitude more powerful than Rayleigh backscattering (Tong et al., 2018; Li et al., 2020). The technique that combines φ-OTDR with UWFBGs is called FBG-Assisted φ-OTDR. In Figure 2.8, Rayleigh backscattered signal is seen like an AC noise superposed on the reflected signal from an UWFBG. Note that the length of UWFBG is assumed to be much shorter than the pulse width so that the length of the reflected section (between 10th and 12th meters) in the trace is equal to spatial resolution, $W = 2m$.

UWFBGs inscribed on the fiber under test, can be interrogated by MZ-supported φ-OTDR. If ΔL is adjusted to be equal to the separation L_{FBG} between a UWFBG pair, the reflected signals from UWFBGs would interfere and yield a relatively high signal level at the detectors as illustrated in Figure 2.9.

---

[2] MI arises when the input pump peak power is increased too much. In our case, there is no need for high input power since fiber under test is barely expected to be longer than 1 km. Polarization fading happens in randomly birefringent fibers where there is no control over SOP of the traveling pulse. In our case, SOP is always under control since the sensing mechanism is composed of polarization-maintaining components.

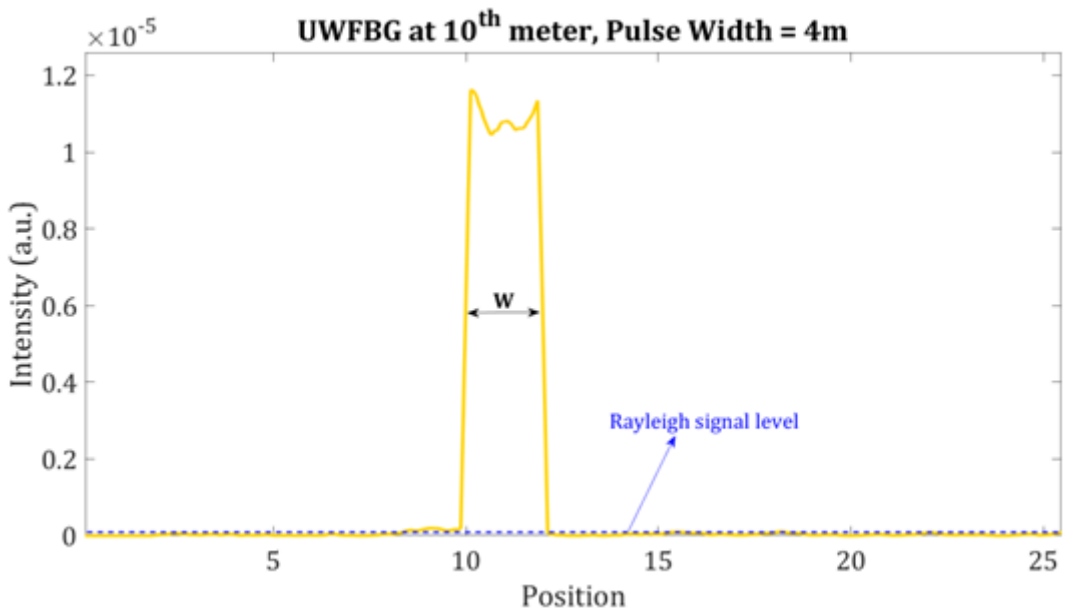

Figure 2.8. FBG-Assisted φ-OTDR power trace where UWFBG is at 10th meter.

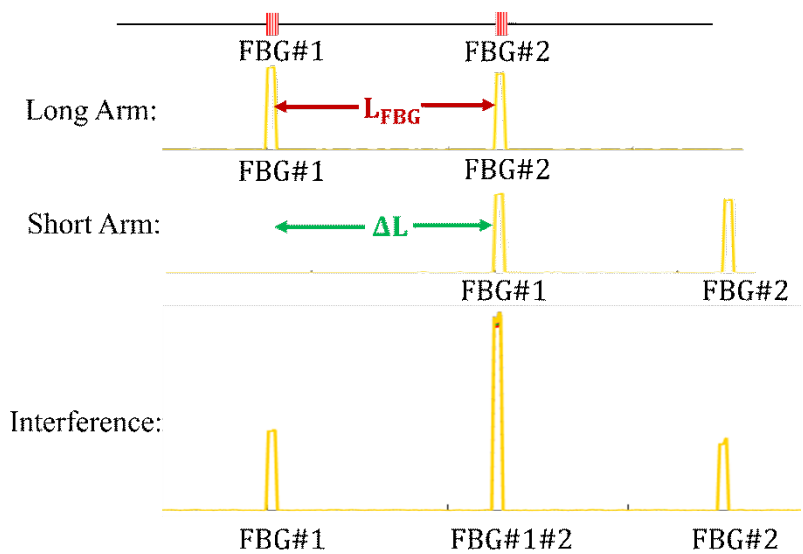

Figure 2.9. Interference of FBG reflections: If arm length difference is equal to the distance between UWFBG pairs, reflected signals interfere.

CHAPTER 3

PROPOSED DESIGN AND MODELLING

As mentioned in Chapter 1, FOCSs use sensing fiber wound around current carrying wire to sense the magnetic field induced by the current according to Ampere' s Law. It exploits Faraday effect whose effects on the fiber birefringence were detailed in Chapter 2. In this chapter, FBG-Assisted φ-OTDR is proposed to interrogate the current-sensing fiber. Then, the model is demonstrated by discrete-time mathematical expressions which are used to develop the simulator tool.

3.1. Design Considerations

φ-OTDR is conventionally used to measure polarization-independent differential phase (phase term that is common for both polarization components) as explained in Section 2.4.1. In current sensing, however, phase shift of interest φ is introduced between the circular polarization components of probe pulse when the only perturbation source is magnetic field induced by the current, H. Note that if the sensing fiber is coiled around the current-carrying wire to constitute a closed loop, the accumulated Faraday phase shift, φ, becomes proportional to the current of interest by Ampere' s theorem as follows:

$$\varphi = 2V \oint H(z)dz = 2VNI \tag{3.1}$$

where V is the Verdet constant, and N is the number of turns around the current carrying wire.

Rayleigh backscattered signal will experience Faraday effect twice, which corresponds to the multiplication of forward and backward Jones matrices obtained from Equation 2.9 by substituting $R_i = 0$, and $\Omega_i = \varphi$.

$$\begin{bmatrix} E_x^0 \\ E_y^0 \end{bmatrix} = \begin{bmatrix} \cos(\varphi) & -\sin(\varphi) \\ \sin(\varphi) & \cos(\varphi) \end{bmatrix} \begin{bmatrix} \cos(\varphi) & -\sin(\varphi) \\ \sin(\varphi) & \cos(\varphi) \end{bmatrix} \begin{bmatrix} E_x^i \\ E_y^i \end{bmatrix} \tag{3.2}$$

$\begin{bmatrix} E_x^0 \\ E_y^0 \end{bmatrix}$ and $\begin{bmatrix} E_x^i \\ E_y^i \end{bmatrix}$ are Jones vectors of the input and output signal. The input SOP can be related to the output SOP by:

$$\begin{bmatrix} E_x^0 \\ E_y^0 \end{bmatrix} = \begin{bmatrix} E_x^i \cos(2\varphi) - E_y^i \sin(2\varphi) \\ E_y^i \cos(2\varphi) + E_x^i sin(2\varphi) \end{bmatrix} \tag{3.3}$$

The phase of output electric fields equals to 2φ if the input polarization state is chosen circular i.e., $E_x^i = 1, E_y^i = \pm j$. In other words, probe pulse must be left or right circularly polarized. Otherwise, there would be a nonlinearity between the applied current and the phase retrieved by φ-OTDR.

For this approach to be valid, linear birefringence must be negligibly small as in low-bi fiber or spun fiber. Due to the advantages of spun fiber mentioned in the previous chapter, it is preferred over low-bi fiber in the design.

In conventional application areas of φ-OTDR such as pipeline monitoring or intrusion detection, true event detection is of first importance, so tolerance range for demodulated phase accuracy is wider than in current measurement applications. Unfortunately, the problem of fading causes φ-OTDR to have percentage error up to 10% which is not acceptable for a reliable current measurement. As mentioned in Section 2.4.3, fading noise can be eliminated by FBG-Assisted φ-OTDR. Since total Faraday phase shift can be obtained by interfering the waves backscattered from before and after the coil, an UWFBG pair can be inscribed ahead and back of the coil.

Another consideration is the perfection of circularly polarized pulse in practice. In general, φ-OTDR is placed far from the sensing coils to ensure thermal, vibrational, and electro-magnetic isolation due to optoelectronic components in it. In this case, circularly polarized pulse may need to be transmitted by a long leading optical fiber which is difficult to be well isolated from environmental effects. Thus, pulse arriving to the sensing coil cannot have a perfect circular SOP in practice. On the other hand, thanks to polarization

maintaining fibers, linear SOP is less deformed during the transmission. Our solution is, therefore, to polarize the pulse linearly (aligned parallel to the slow (x) axis of PMF) by a polarizer that is inserted before the first coupler so that it can be transmitted up to where the current sensing part of the fiber starts. Then, it is converted into the circular SOP by a quarter-wave plate (QWP) spliced with 45-degree and coupled to spun fiber. The resulting design schematic is shown in Figure 3.1.

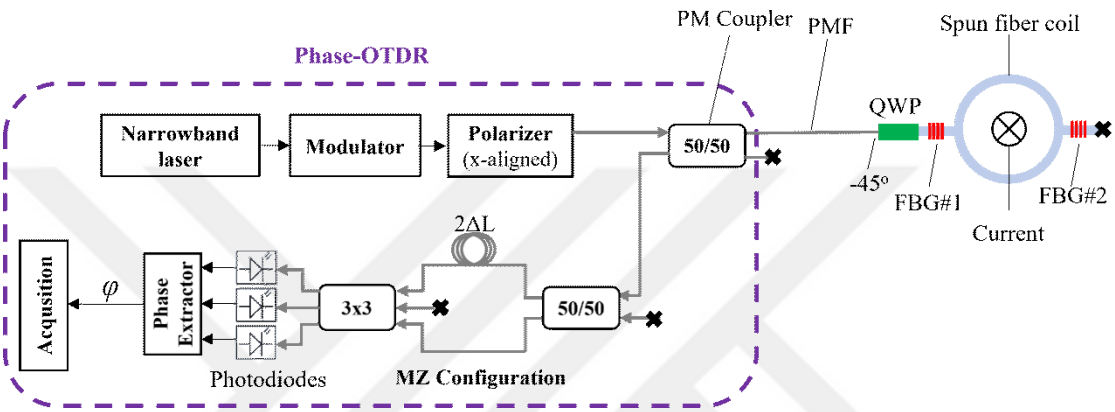

Figure 3.1. Proposed current sensing system

3.2. Jones Analysis of the Proposed Design

Assuming that PMF has a constant linear birefringence δ_0 aligned with the input polarizer (ϕ=0) and a length of L_0, the total retardance becomes $R = \delta_0 L_0$. From Equation 2.9, its Jones matrix becomes:

$$J_{PMF} = \begin{bmatrix} e^{j\delta_0 L_0/2} & 0 \\ 0 & e^{-j\delta_0 L_0/2} \end{bmatrix} \tag{3.4}$$

Jones matrix of QWP that is aligned with 45 degrees can be derived from again Equation 2.9, regarding it as a fiber section with a retardance of 90 degrees. The resulting matrix becomes

$$J_{QWP} = \frac{1}{\sqrt{2}} \begin{bmatrix} 1 & j \\ j & 1 \end{bmatrix} \tag{3.5}$$

Assuming the input probe pulse is x-polarized, SOP of the signal arriving to spun fiber, V_{insp} can be obtained as RCP:

$$V_{insp} = J_{QWP} \times J_{PMF} \times \begin{bmatrix} 1 \\ 0 \end{bmatrix} = A_0 \begin{bmatrix} 1 \\ j \end{bmatrix} \tag{3.6}$$

where $A_0 = \frac{1}{\sqrt{2}} e^{j\delta_0 L_0/2}$.

Since the spun fiber is ideally circular birefringent, SOP of the back-reflected signals from first (one before the coil) and second (one after the coil) FBGs would be maintained circularly polarized. The signal reflected from the second one would be carrying the Faraday phase shift φ. When they arrive at the intersection of spun fiber and QWP, their Jones vector expressions would be

$$V_{outsp1} = A_1 \cdot \begin{bmatrix} 1 \\ j \end{bmatrix} \tag{3.7}$$

$$V_{outsp2} = A_2 \cdot \begin{bmatrix} 1 \\ j \end{bmatrix} e^{j2\varphi} \tag{3.8}$$

where A_1 and A_2 are complex constants related to A_0, FBG parameters and transmission parameters of spun fiber. After passing through QWP in the backward direction, the SOPs will be linear, so PMF will transmit them to 3×3 coupler almost without any SOP deformation. Jones vector of the signals that arrive at 3×3 coupler can be given by

$$V_{back1} = J_{QWP} \times V_{back1} = \hat{A}_1 \begin{bmatrix} 0 \\ 1 \end{bmatrix} \tag{3.9}$$

$$V_{back2} = J_{QWP} \times V_{back2} = \hat{A}_2 \begin{bmatrix} 0 \\ 1 \end{bmatrix} e^{j2\varphi} \tag{3.10}$$

where $\hat{A}_1$ and $\hat{A}_2$ are complex constants related to A_1, A_2, transmission parameter of QWP, couplers and the PMF. After the interference at 3×3 coupler, phase difference between V_{back1} and V_{back2}, appears in the amplitude of the detector outputs along with the $2\pi/3$ rad phase offsets such as:

$$\begin{aligned} P_1 &= K + M\cos(\alpha + 2\varphi) \\ P_2 &= K + M\cos\left(\alpha + 2\varphi - \frac{2\pi}{3}\right) \\ P_3 &= K + M\cos\left(\alpha + 2\varphi + \frac{2\pi}{3}\right) \end{aligned} \tag{3.11}$$

where $\alpha = \angle\hat{A}_2 - \angle\hat{A}_1$. Note that the only pulse to pulse varying parameter in the phase difference is φ. Thus, α can be measured when the current is off.

After removing the DC term $K = \frac{P_1+P_2+P_3}{3}$, phase can be extracted using trigonometric identities as follows:

$$\varphi_{ext} = \frac{1}{2}\left[\arctan\left(\frac{P_2 - P_3}{\sqrt{3}P_1}\right) - \alpha\right] \tag{3.12}$$

Finally, φ_{ext} is multiplied by a scale factor $\frac{1}{2VN}$ according to Equation 3.1 to get the current of interest.

3.3. Sensor Calibration

The sensing principle described in the previous section ignores the linear birefringence. However, spun fibers available on the market are manufactured from high-birefringent preforms to minimize the externally induced linear birefringence due to packaging, bending, etc. Therefore, the scale factor becomes a function of the applied current,

which results in a nonlinear relation between φ_{ext} and I. In order to suppress this nonlinearity error, we propose a calibration process that takes place by interrogating at least one known current with φ-OTDR to obtain a scale factor $\mathbb{K}(I_0)$ as the ratio of the calibration current I_0 to the resulting phase $\varphi(I_0)$:

$$\mathbb{K}(I_0) = \frac{I_0}{\varphi\left(I_0\right)} \tag{3.13}$$

Let I_x to be the current to be measured, so the demodulated phase is $\varphi(I_x)$. When $\mathbb{K}(I_0)$ is used to convert the demodulated phase $\varphi(I_x)$ to the current i.e., $\mathbb{K}(I_0)\varphi(I_x)$, the error; defined as the normalized difference between measured to the applied current would become:

$$\epsilon = \frac{I_x - \mathbb{K}(I_0)\varphi(I_x)}{I_x} \tag{3.14}$$

Substituting I_x with $\mathbb{K}(I_x)\varphi(I_x)$, the error is found out to be the error between the scale factors i.e.:

$$\epsilon = \frac{\mathbb{K}(I_x) - \mathbb{K}(I_0)\varphi(I_x)}{\mathbb{K}(I_x)} \tag{3.15}$$

This error can be reduced by calibrating with as many current amplitudes as possible. Thanks to the fast response of φ-OTDR, sweeping the current from minimum to maximum value in the sensing range allows a quick (less than a second) and precise (around 1 A sampling rate) calibration in a wide range (0-100s of kA), if the source is capable of a linear sweeping in a controllable manner. If such a source is not available, an alternative method is to determine the scale factors for only a few currents and approximate the scale factor as a linear function of the applied current.

3.4. Simulator Tool Development

There are a few studies on the development of mathematical model for φ-OTDR, in the literature (Liokumovich et al., 2015; Masoudi and Newson, 2017a; Wojcik, 2006;

Kocal, 2021; Brown, 2017), but none of them explicitly demonstrates how to include the polarization effects. In this section, first, one-dimensional impulse response model for φ-OTDR is presented. Then, the polarization effects are taken into account and lastly, FBGs are included.

3.4.1. Backscattering Model without Polarization Effects

φ-OTDR model without polarization effects is implemented mostly based on the approach demonstrated in (Liokumovich et al., 2015). According to this approach, fiber is considered in one dimension and divided into subparts, so called "scattering interval", with equal length of D. A vast number of microscale Rayleigh scatterers lying inside each interval are represented by a single milli-scale scattering center which has a random amplitude a_k with Rayleigh distribution and a random position z_k with uniform distribution between the boundary positions of its scattering interval as shown in Figure 3.2. For the model to be valid, D must be much smaller than the spatial resolution so that the statistical properties of Rayleigh backscattering still hold (Masoudi and Newson, 2017a).

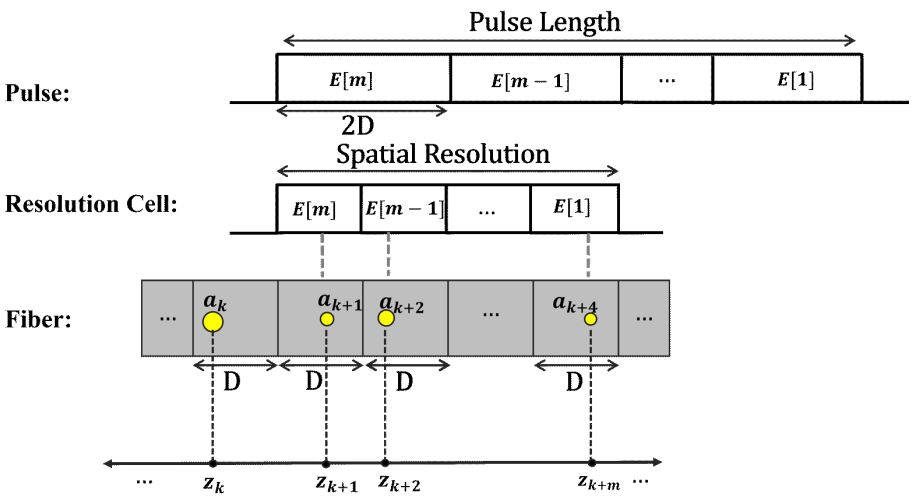

Figure 3.2. Pulse and fiber models. Pulse is assumed to be moving rightward.

Assuming the variation of attenuation due to the random position of scattering centers in each interval is negligible, the fiber model can be represented in discrete domain

as follows:

$$Fib[k] = \sum_{i=1}^{N} a_i \exp\{2j\beta z_i\}\delta[k-i] \tag{3.16}$$

where k is the discrete index, N is the number of scattering centers, β is the propagation constant and $\delta[x]$ is the discrete Dirac delta function that equals to 1 or 0 if x is zero or non-zero, respectively. Distribution of a_i obeys Rayleigh with a mean of μ_a:

$$\mu_a = \sqrt{\frac{\pi B_R D}{4}} \tag{3.17}$$

where B_R is the Rayleigh backscattering coefficient, equal to $3.2 \times 10^{-8} m^{-1}$ for a single mode fiber at 1550 nm (Beller, 1998).

Pulse is modelled by m spatial electric field elements so that the resolution cell covers m scattering centers at once, as illustrated in Figure 3.2. The elements are complex numbers with an amplitude $E[k]$ decided by the peak power and the shape (waveform). Their phase is assigned by assuming that the coherence length of the pulse is much higher than the pulse width (phase information of each element remains perfectly correlated). Noting that the physical distance between adjacent elements of pulse is $2D$ rather than D (due to round-trip time), resulting model can be expressed in discrete form as follows:

$$Pulse[k] = \sum_{i=1}^{m} E[i] \exp\{-2j\beta i D\}\delta[k-i] \tag{3.18}$$

Note that the first index of pulse ($Pulse[1]$) enters the fiber first. Therefore, the backscattered electric field $EF[k]$ can be found by the discrete convolution of $Fib[k]$ and $Pulse[k]$:

$$EF[k] = Fib[k] * Pulse[k] \tag{3.19}$$

which can be expressed in open form as:

$$EF[k] = \sum_{u=m}^{N} \sum_{i=1}^{m} a_{u-i+1} E[i] \exp\{2j\beta z_{u-i+1} + 2j\beta i D\} \delta[k-u] \tag{3.20}$$

For simplicity, backscattering occurred before the pulse entirely entered the fiber is ignored, so u starts from m.

Then, the backscattered signal intensity can be calculated as:

$$I[k] = |EF[k]|^2 \exp\{-2\alpha k D\} \tag{3.21}$$

where α is the attenuation constant[1]. If electric field amplitude $|EF|$ is assigned as the square root of the input pulse power, the intensity calculated in Equation 3.21 corresponds to power.

3.4.2. Jones Matrix of Optical Fiber

A common approach for modelling a fiber is to consider it as "a series of fiber elements" each with uniform polarization properties and equal length. Each element can be modelled by Jones matrix in Equation 2.9. Retardance B_k and rotation Ω_k must be related to the physical parameters of the kth element such as its length (ℓ), intrinsic birefringence (δ_k), spin rate (ξ_k) and Faraday phase shift per unit length ($\theta_k = \frac{d\varphi}{dz}|_{z=k\ell}$). If the only linear birefringence is intrinsic, the effective retardance is expressed by:

$$B_k = \frac{R_k}{2} e^{j2\phi_k} \tag{3.22}$$

where ϕ_k is the azimuthal angle of intrinsic birefringence. R_k, Ω_k and ϕ_k are defined as (Barlow et al., 1981):

[1] Attenuation is usually included in Equation 3.16, but implicitly assuming that the attenuation does not change significantly along the resolution cell, it can be added while calculating intensity.

$$R_k = 2\arcsin\left[\frac{\delta_k}{2\sqrt{\frac{\delta_k^2}{4}+(\xi_k-\theta_k)^2}}\sin\left(\ell\sqrt{\frac{\delta_k^2}{4}+(\xi_k-\theta_k)^2}\right)\right] \tag{3.23}$$

$$\Omega_k = \xi_k\ell + \arctan\left[\frac{\theta_k-\xi_k}{\sqrt{\frac{\delta_k^2}{4}+(\xi_k-\theta_k)^2}}\tan\left(\ell\sqrt{\frac{\delta_k^2}{4}+(\xi_k-\theta_k)^2}\right)\right] \tag{3.24}$$

$$\phi_k = \frac{(2k-1)\,\xi_k\ell - \Omega_k}{2} + q_0 \tag{3.25}$$

where q_0 is the azimuth at the beginning of the fiber.

Assuming the operation wavelength is 1550 nm, bending the fiber with a radius of r induces an external linear birefringence b_k^B that is $2.162\times10^{-3}/r^2$. Another external linear birefringence source is FBG, since during its inscription, one side of the fiber is exposed to UV light more than the other side. Consequently, it brings an FBG-induced birefringence b_k^F that is generally between $40.54-405.4$ rad/m. They can be included in the Jones matrix by updating the effective retardance as:

$$B_k = \frac{R_k}{2}e^{j2\phi_k} + \frac{b_k^B\ell}{2}e^{j2q_k^B} + \frac{b_k^F\ell}{2}e^{j2q_k^F} \tag{3.26}$$

where q_k^B and q_k^F are the azimuthal angles of bending- and FBG-induced birefringence, respectively.

The scope of this thesis does not include the effect of fiber twists on the results. Also, in general, twist can be avoided more easily Therefore, it is not included in the model, but its expression can be found in (Dandu et al., 2022).

For backward Jones matrix, sign of ξ is reversed, so forward and backward Jones matrices of unspun and untwisted fibers are the same. Yet, we will denote the forward and backward Jones matrices of kth section with $\overrightarrow{J_k}(\ell)$ and $\overleftarrow{J_k}(\ell)$ for clarity.

3.4.3. Revised Backscattering Model with Polarization Effects

For PMF, scattering intervals with length D in the backscattering model can be assumed to have uniform polarization characteristic. Thus, we can choose the element length as $\ell = D$. Then the Jones matrix of kth scattering interval can be denoted as $\overrightarrow{J_k}(D)$ and $\overleftarrow{J_k}(D)$ for forward and backward directions. Light with Jones vector V_i arriving at the scattering center with position z_k in the kth element experiences first $k-1$ consecutive intervals and a partial section of kth interval with a length of $z_k - (k-1)D$. Eventually, its resulting state of polarization becomes $\overrightarrow{J_k}\left(z_k - (k-1)\,D\right) \times \overrightarrow{J_{k-1}}\left(D\right) \times \ldots \overrightarrow{J_2}\left(D\right) \times \overrightarrow{J_1}\left(D\right) V_i$. Therefore, the transfer matrix for the forward propagation up to k^{th} interval can be defined as an array of 2×2 matrices as follows:

$$\overrightarrow{T}[k] = \sum_{u=1}^{N} \overrightarrow{J_u}\left(z_u - (u-1)\,D\right) \times \overrightarrow{J_{u-1}}\left(D\right) \times \ldots \overrightarrow{J_1}\left(D\right) \delta\left[k-u\right] \tag{3.27}$$

Similarly, a transfer matrix for the reverse direction can be written as:

$$\overleftarrow{T}\left[k\right] = \sum_{u=1}^{N} \overleftarrow{J_1}(D) \times \overleftarrow{J_2}(D) \times \ldots \overleftarrow{J_u}(z_u - (u-1)D)\delta[k-u] \tag{3.28}$$

Eventually, overall transfer matrix $T[k]$ can be defined as $T[k] = \overleftarrow{T}[k] \times \overrightarrow{T}[k]$. Fiber model can be rewritten by including the transfer matrix into Equation 3.16:

$$Fib[k] = \sum_{i=1}^{N} a_i T\left[i\right] \exp\left\{2j\beta z_i\right\} \delta\left[k-i\right] \tag{3.29}$$

Pulse with two polarization components can be expressed as a 2-D array with a size of $2 \times m$:

$$Pulse[k]^2 = \sum_{i=1}^{m} \begin{bmatrix} E_x[i] \\ E_y[i] \end{bmatrix} \exp\{2j\beta iD\}\delta[k-i] \tag{3.30}$$

Then, the resulting electric field can be obtained by a similar operation described in the first part. In this case, however, the convolving points will be corresponding to a 2×2 matrix and a 2×1 vector.

$$EF\,[k] = \sum_{u=m}^{N} \sum_{i=1}^{m} Fib\,[u-i+1] \times Pulse\,[i]\delta\,[k-u] = \begin{bmatrix} EF_x[k] \\ EF_y[k] \end{bmatrix} \tag{3.31}$$

If there is not a polarization splitting before the detection, the intensity becomes:

$$I\,[k] = |EF_x\,[k] + EF_y\,[k]|^2 \exp\{-2\alpha kD\} \tag{3.32}$$

For spun fibers, however, spin pitch, defined as $\frac{2\pi}{\xi}$, must be much smaller than ℓ. In our design, scattering interval length and spin pitch are comparable to each other, so the condition of $\ell \ll D$ must be satisfied. Therefore, the intervals are separated into micro segments as illustrated in Figure 3.3.b and Jones matrix of each segment is found from Equation 2.9. The number of micro-segments must be high enough for the model to converge towards the true Jones matrix of the interval. The optimum number for this study is decided to be 250, regarding both the computational efficiency and the convergence rate.

3.4.4. Adding FBG to the Model

Rayleigh backscattering in FBG-inscribed intervals is negligible compared to the FBG reflection. Thus, the scattering center in an FBG-inscribed interval is canceled and an FBG reflection center is placed at the end of the interval. Since FBG length is assumed

[2] $Pulse$ is a $2 \times m$ matrix, so $Pulse[k]$ represents its kth column which is a 2×1 vector.

to be shorter than an interval length, FBG reflection amplitude is a function of FBG length (L_{FBG}) rather than the interval length i.e.:

$$r = \frac{-\kappa \, sinh(\alpha L_{FBG})}{\hat{\sigma} \sinh(\alpha L_{FBG}) + j\alpha \cosh(L_{FBG})} \tag{3.33}$$

where $\alpha = \sqrt{\kappa^2 - \hat{\sigma}^2}$; $\kappa = \frac{\pi}{\lambda}\delta n$; $\hat{\sigma} = \delta + \sigma$; $\delta = 2\pi n_{eff}\left(\frac{1}{\lambda} - \frac{1}{\lambda_B}\right)$; $\sigma = \frac{2\pi}{\lambda}\delta n$; λ is the wavelength, and δn is the index modulation.

In our proposed sensor setup FBGs are inscribed on spun fiber which is modelled by micro-segmenting. FBGs cover only few micro segments due to their short length. Since their positions are deterministic, they are assumed to be at the end of the interval that they are written on. Thus, FBG-induced birefringence is included in the Jones matrices of the micro segments covered by them as illustrated in Figure 3.3.c.

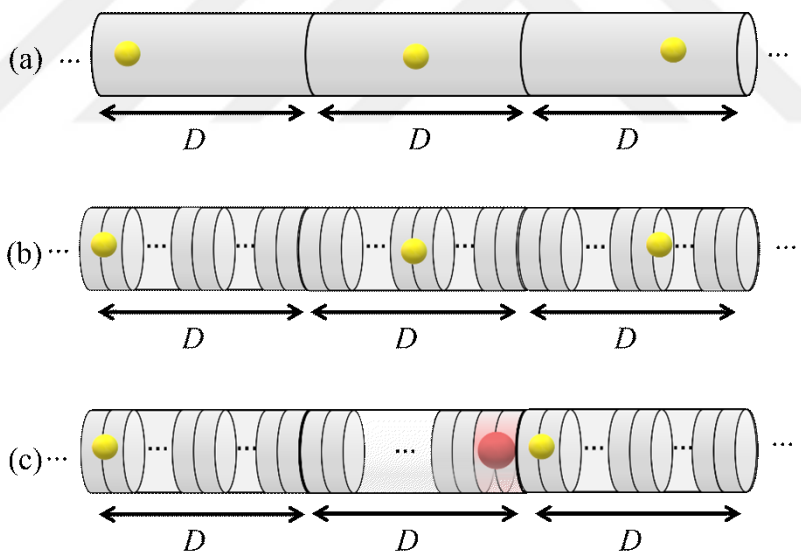

Figure 3.3. Scattering interval models for a) PMF, b) spun fiber, c) spun fiber with an FBG inscribed on the interval in the middle. Yellow dots represent the scattering centers. Red dot represents FBG reflection center.

CHAPTER 4

RESULTS AND DISCUSSION

In this chapter, results obtained from the simulation tool are presented and discussed.

4.1. Tracing the SOP via Poincaré Sphere

Fiber models are verified by drawing the evolving SOP on the Poincaré Sphere as light travels forward and scatters back. When x-polarized input light is sent through two spun fibers with the same beat length of 5 m and spin pitches of 2 m and 0.5 m, its SOP evolves in forward direction as illustrated with pink trace in Figure 4.1. After it backscatters from 4th meter, its SOP evolves in backward direction drawn in light blue. Red, orange, and blue dots show the initial, after forward propagation and final SOPs. The results match up with a previous study on modelling spun fiber (Jovicic, 2020).

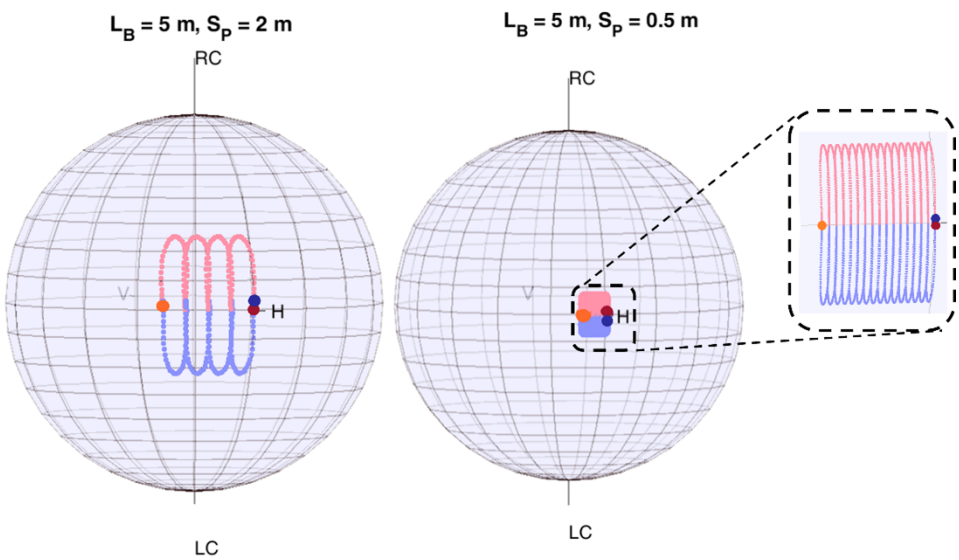

Figure 4.1. Change of SOP as light propagates forward and backscatters.

The design in Section 3.1 consists of PMF, QWP, and spun fiber which are connected successively. Their parameters are given in Table 4.1.

Table 4.1. Fiber parameters

Fibers	**Length**	**Beat Length**	**Spin Pitch**
PMF	10 m	2 mm	inf
QWP	5 cm	20 cm	inf
Spun Fiber	5 m	1 cm	2.5 mm

When the input is x-polarized, its SOP evolution is simulated as shown in Figure 4.2 with 2.5 mm steps as it propagates forward and guided back by backscattering at the end of the line.

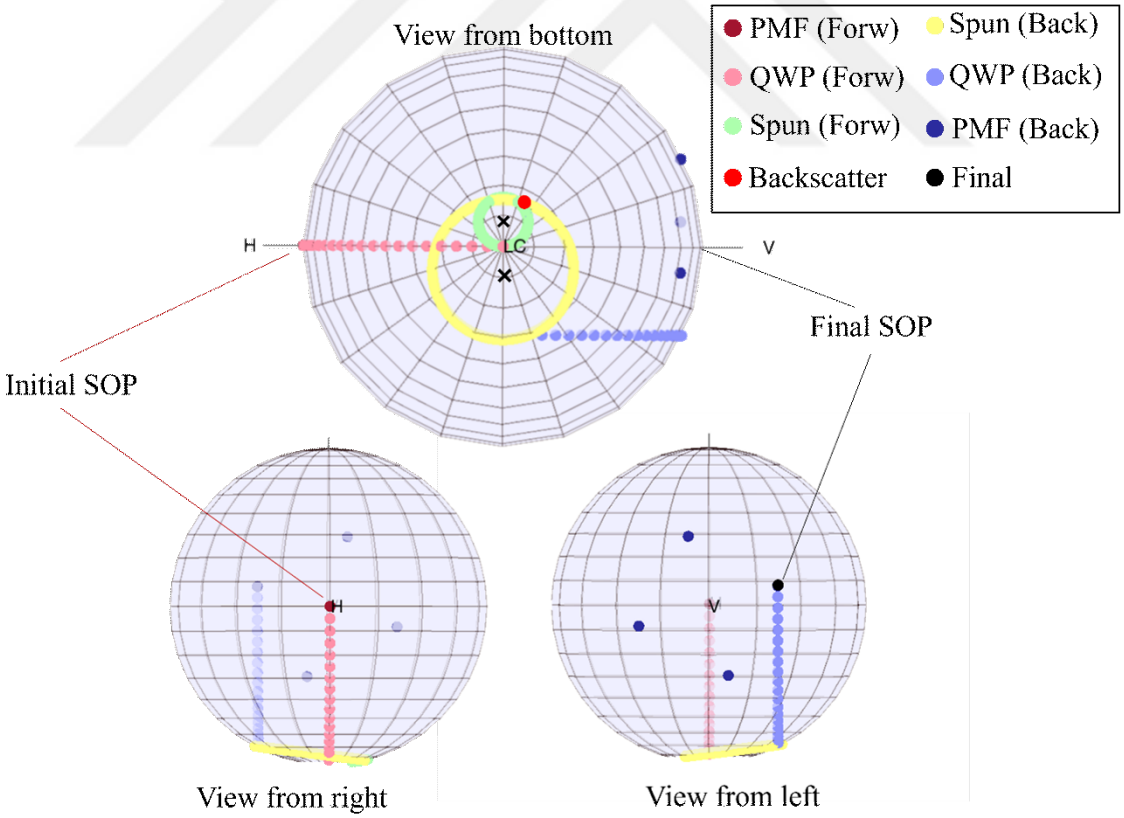

Figure 4.2. SOP evolution along the proposed fiber line

Claret red point seen from right indicates the initial horizontally polarized state, so it is on the H point of Poincaré Sphere. Since PMF maintains the SOP, it does not move until light arrives at the QWP. As light passes through QWP, its SOP starts to change as traced by light red points. When it becomes LCP, light is coupled to the spun fiber, in which it evolves as drawn by light green points. Since the spun fiber has a comparable linear birefringence with its spin rate, SOP traces the green circle rather than remaining on LC. Note that the center of the circle marked with a green cross corresponds to the elliptical birefringence axis of the spun fiber in forward direction. At the instance of backscattering, SOP is shown with orange point. In backward direction, SOP evolves along the yellow circle which has a center (indicated with a black cross) that is symmetrical to the center of the green circle with respect to the intrinsic spun fiber linear birefringence axis. It is because the forward and backward Jones matrices of spun fiber differs only by the sign of the effective rotation, assuming no externally induced birefringence sources are present. The radius of the circles depends on the SOP that light has when it is coupled to the spun fiber.

The QWP converts the circular-like elliptical SOP coming from the spun fiber into a linear-like SOP. Since the SOP arrived back the PMF is no longer linearly polarized, it makes a circle around the vertical birefringence axis. Since the beat length of PMF is smaller than the simulation step, only 4 points of the circle can be observed as indicated by blue points in Figure 4.2. Final SOP can be any of the blue points, depending on the PMF length.

If the intrinsic beat length of the spun fiber is increased to 10 cm, the resulting SOP evolution is given in Figure 4.3. Final SOP is almost vertically polarized which provides more accurate and linear sensor response.

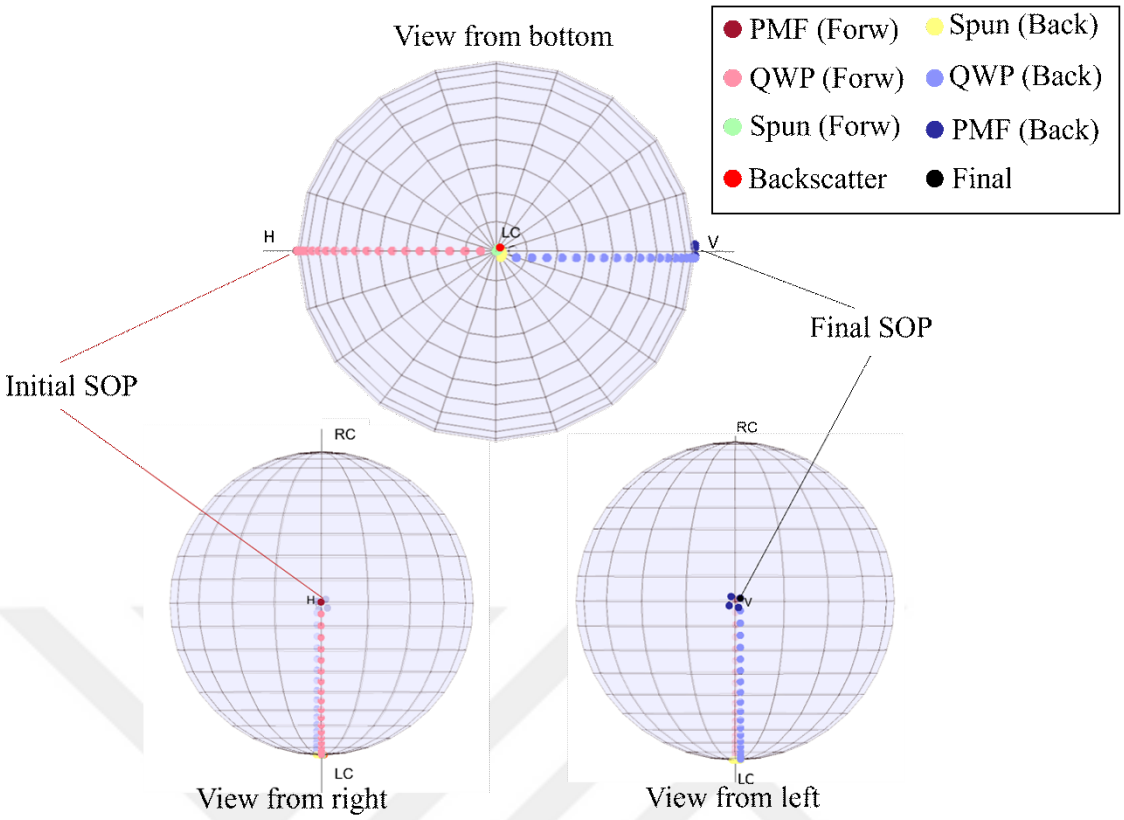

Figure 4.3. SOP evolution along the proposed fiber line

4.2. φ-OTDR Simulation Results

In this section, current sensing system via φ-OTDR proposed in Section 3.1 is simulated without FBGs. The design setup is given in Figure 4.4. Fiber parameters are as in the Table 4.1 except the length of spun fiber that is 20 meters, including the sensing coil with a radius of 0.1 m and 8 turns. Coil starts at 13th meter and ends at $\sim 18^{th}$ meter. Scattering interval length D is 2.5 mm. Spun fiber is modelled by separating its scattering intervals to 250 micro-segments as described in the last paragraph of the Section 3.4.3. Pulse length is 2 m, providing a spatial resolution of 1 m. Imbalanced path length $2\Delta L$ is 14 m. Current values during 4 pulse shots are 0, 5, 10 and 15 kA, respectively.

Rayleigh backscattering power trace detected by the three detectors is given in Figure 4.5.

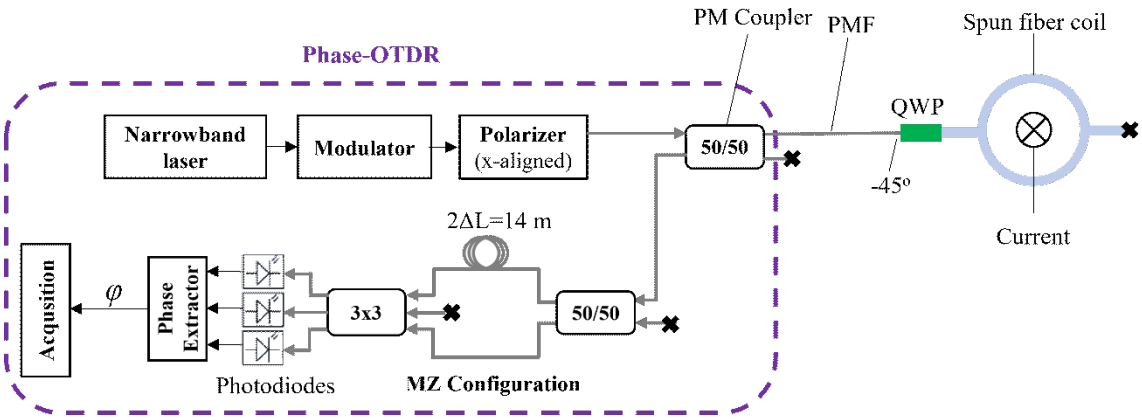

Figure 4.4. Sensing setup without FBGs.

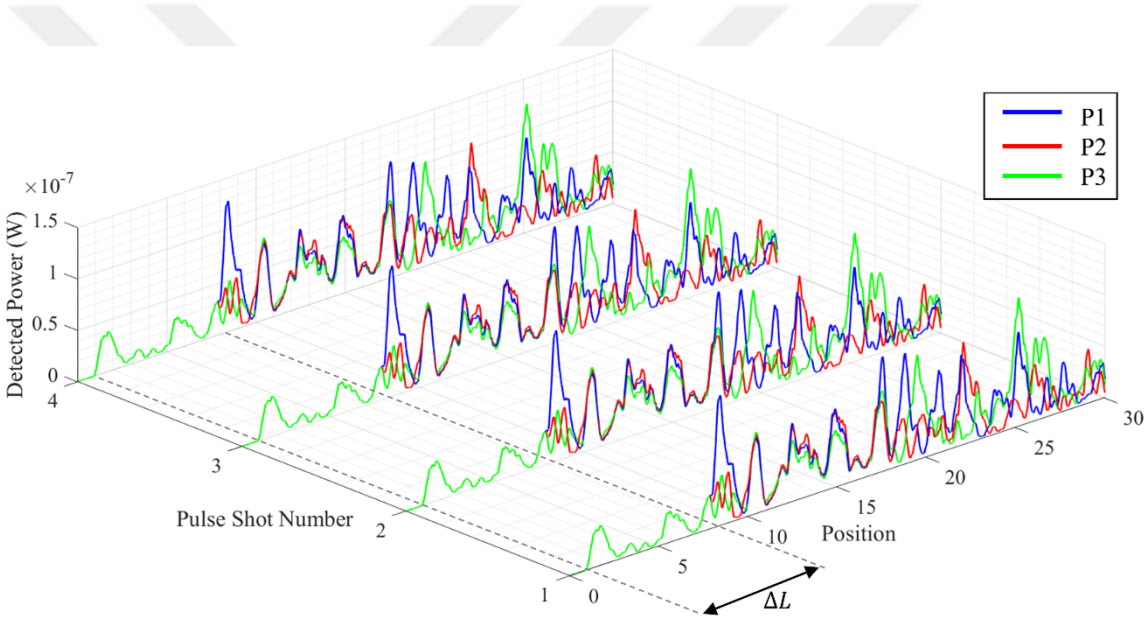

Figure 4.5. Rayleigh backscattering power detected by the three detectors.

Backscattered electric field is not calculated as long as pulse is totally in the fiber. Therefore, first 1 meter (corresponding to the length of resolution cell) of the trace is filled with zeros. In between 1st and 8th meters, no output comes from the delayed arm of IMZI, since the imbalanced path length is 14 m. Thus, detectors receive the signal from non-delayed arm only. Since no interference occurs between the delayed and non-delayed waves, the interference term M in Equation 3.11 becomes zero and the detected power by the three detectors are equal in between 1st and 8th meters.

The signal arriving at IMZI (before it arrives) is a superposition of many waves scattered from the different parts of the pulse, which also interfere with each other. This phenomenon known as "the interference fading" is the reason of the jaggy appearance of the power trace.

Phase trace given in Figure 4.6 is computed from the detector outputs by Equation 3.12.

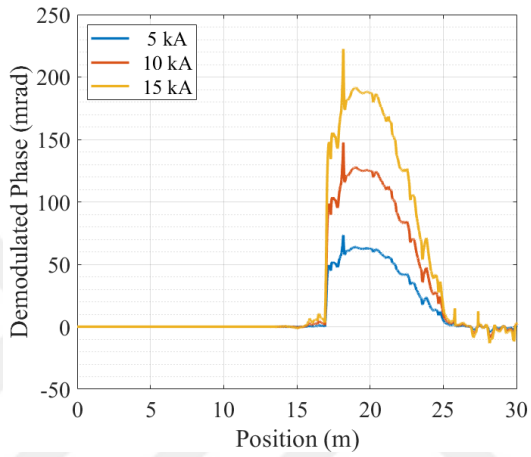

Figure 4.6. Demodulated phase trace.

Total Faraday phase shift can be read from the measurement zone, that is between 19th and 21st meters of the demodulated phase trace, as explained in Section 2.4.2. The reason behind the ripples on the trace is the interference fading. Total Faraday phase can be obtained by averaging the phase in the measurement zone, which may lessen the impact of the unwanted fluctuations. The applied and demodulated phases are given in Table 4.2.

Table 4.2. Comparison of expected and demodulated phase

Current	**Total Faraday Phase**	**Demodulated Phase**	**Error %**
5 kA	0.064	0.0627	2.03
10 kA	0.1280	0.1255	1.95
15 kA	0.1919	0.1882	1.93

The percentage error is calculated by:

$$Error\% = \frac{\varphi_{TotalFaraday} - \varphi_{Demodulated}}{\varphi_{TotalFaraday}} \times 100 \tag{4.1}$$

4.3. FBG-Assisted φ-OTDR Simulation Results

In order to mitigate the interference fading noise to increase the accuracy, the design is updated by including two FBGs before and after the sensing coil. The setup is illustrated in Figure 4.7. The received power trace is given in Figure 4.8.

The middle peaks in Figure 4.8 correspond to the interference zone that is between 19.5^{th} and 20.5^{th} meters. The dashed rectangle in the trace of 4th shot shows the Rayleigh backscattering level that is much lower than the reflection level. Also, the intensity variation along the position axis in the peaks is due to Rayleigh backscattering.

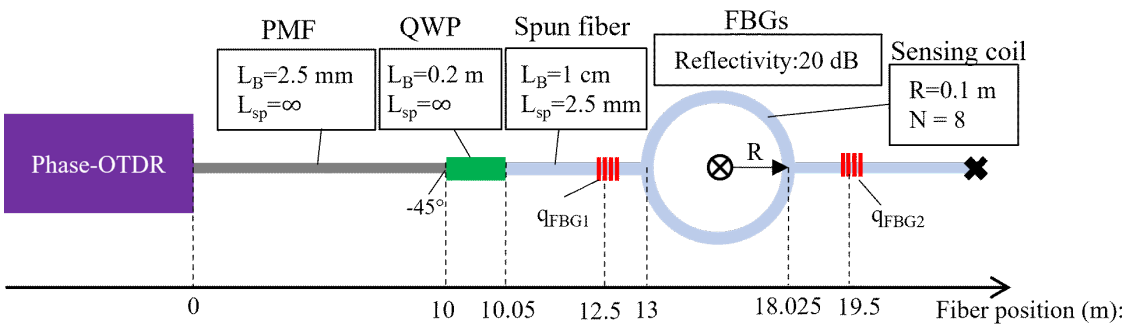

Figure 4.7. Sensing setup when FBGs are included.

The demodulated phase trace is given in Figure 4.9. The FBG interference zone zoomed-in in the dashed rectangle is free of ripples since the SNR of the received signal from there is much higher thanks to the FBGs. The phase values in that zone are averaged to get the total Faraday phase. The comparison of the demodulated and applied phase is given in Table 4.3.

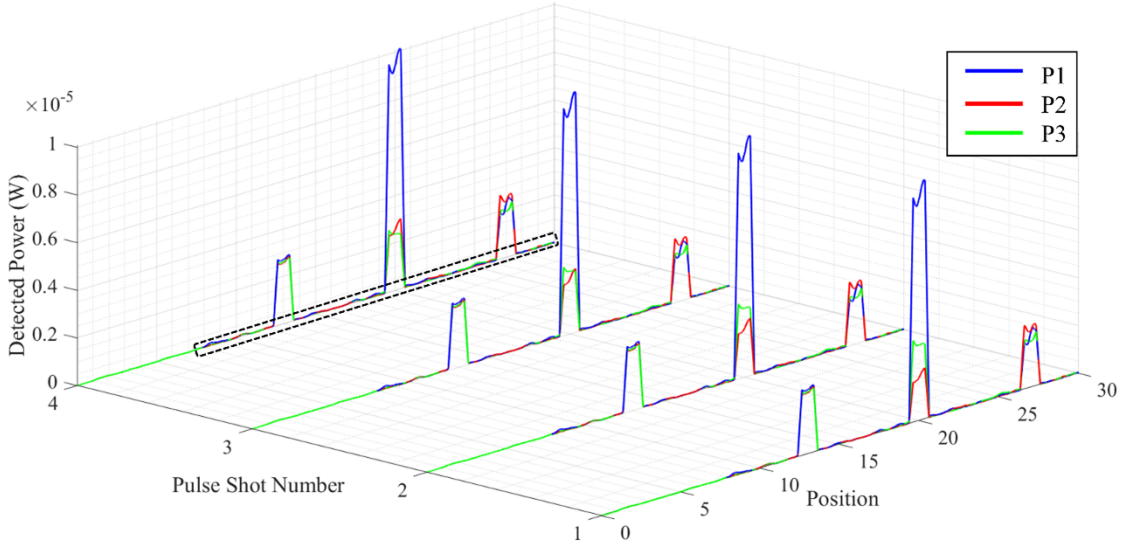

Figure 4.8. Backscattered and reflected signal power received by the three detectors.

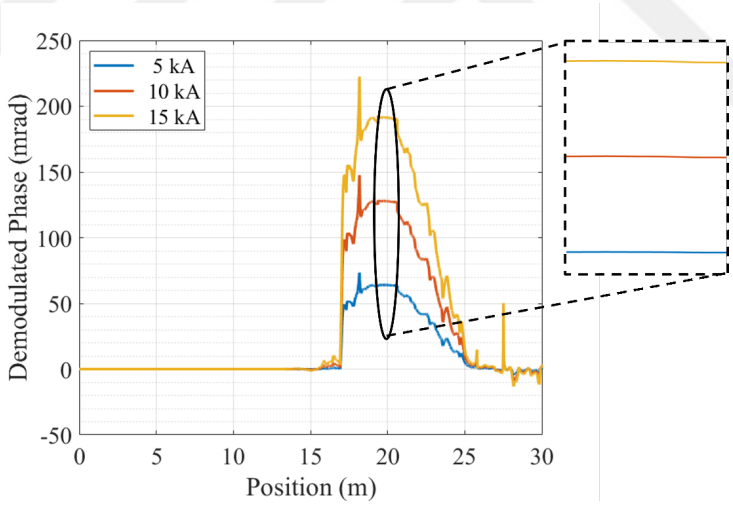

Figure 4.9. Demodulated phase trace when FBGs are included.

The percentage error fell below 0.5% after FBGs are added. However, these rates are still too much for electric current applications in general. The remaining error source is the nonlinearity induced by the intrinsic linear birefringence of spun fiber. Additionally, there may be external birefringence sources which will be analyzed later.

As explained in Section 3.3, the sensor nonlinearity can be diminished by a calibration process. Ideally, scale factor as the ratio of applied current to the demodulated

Table 4.3. Comparison of expected and demodulated phase when FBGs are included

Current	**Total Faraday Phase**	**Demodulated Phase**	**Error %**
5 kA	0.064	0.0639	0.19
10 kA	0.1280	0.1276	0.31
15 kA	0.1919	0.1911	0.43

phase is a function of V and N. However, in hi-bi spun fibers, it is also a function of applied current as well as the beat length and the spin pitch as shown in Figure 4.10 by red dots. If the calibration is done with a single current in the middle of the range, it can be approximated as a constant (like the green dashed horizontal line). However, it can cause up to 0.5% nonlinearity error between the sensing limits. Calibration with multiple currents, on the other hand, can provide a more accurate linear approximation. If only the minimum and maximum currents are used to calibrate, the scale factors between them can be approximated by a line fitting. Such an approximation, given by blue line, results in a nonlinearity error up to 0.04%. Regarding the noise and other possible imperfections during the calibration, it is safer to calibrate with as many currents as possible. Black line is obtained by calibrating with 5 current values indicated by black crosses, which suppresses the error below 0.01%.

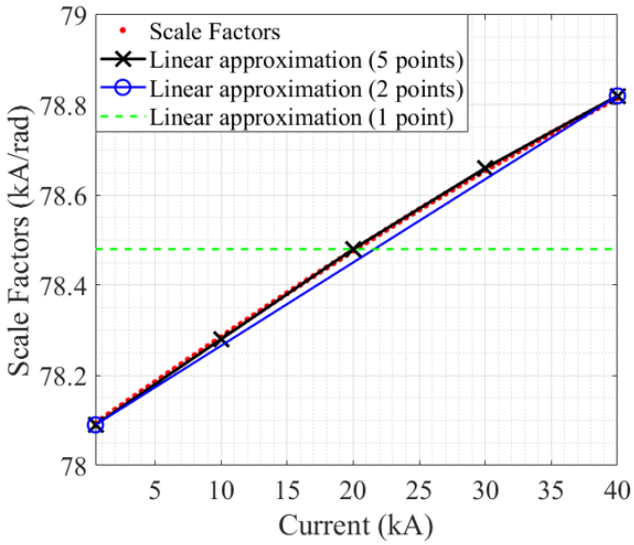

Figure 4.10. Linear approximation to the scale factors

4.4. Orientation of FBG and Coil Bending

Scale factor varies with FBG and bending orientation when we include FBG- and bending-induced linear birefringence. Their effect is examined separately by increasing current from 4 kA to 16 kA (indicated by different colors).

When FBG angles are swept from 0 to 180 degrees by a step of 9 degrees, the resulting scale factors are plotted as a surface in Figure 4.11. When bending angle is swept in the same way, resulting scale factors are plotted in Figure 4.12.

As current changes, scale factor graphs are proportionally moved in vertical direction while their shape is substantially preserved. Although there is a slight horizontal shift, rate of change with respect to current (in vertical direction) is almost constant. Therefore, it can be successfully estimated by calibrating with more than one current value. Then, as long as the orientations stay static, the orientation angles will have no significance at all.

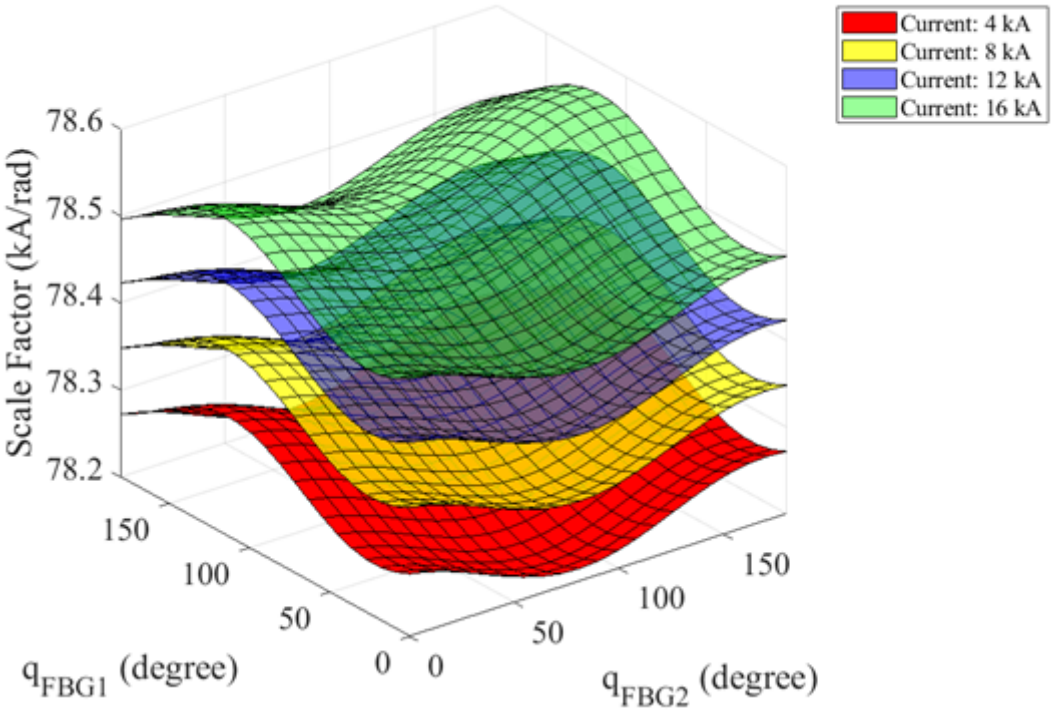

Figure 4.11. Effect of FBG orientations on the scale factor

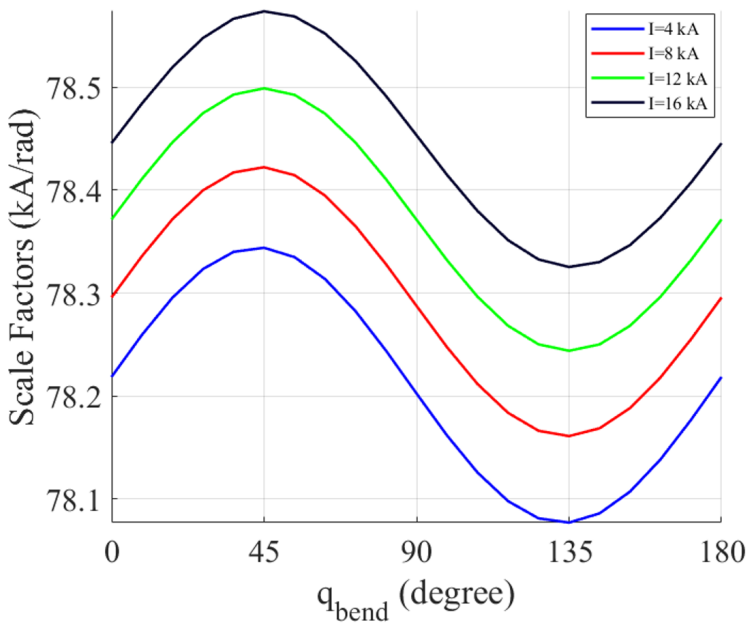

Figure 4.12. Effect of bending orientation on the scale factor

4.5. Detector Noise Effect

Scale factors, taking into account the noise of the three detectors, are plotted for currents ranging from 1 kA to 40 kA in Figure 4.13 (blue dots and standard deviation). The red line indicates the noiseless case which shows a linear behavior. The deviations were obtained by 20 trials. It shows that the current values near zero are more impacted by the noise. For currents equal or higher than 1 kA, the deviation falls under 1%. Especially for a healthy calibration, the minimum calibration current must be large enough for a better fitting of scale factor.

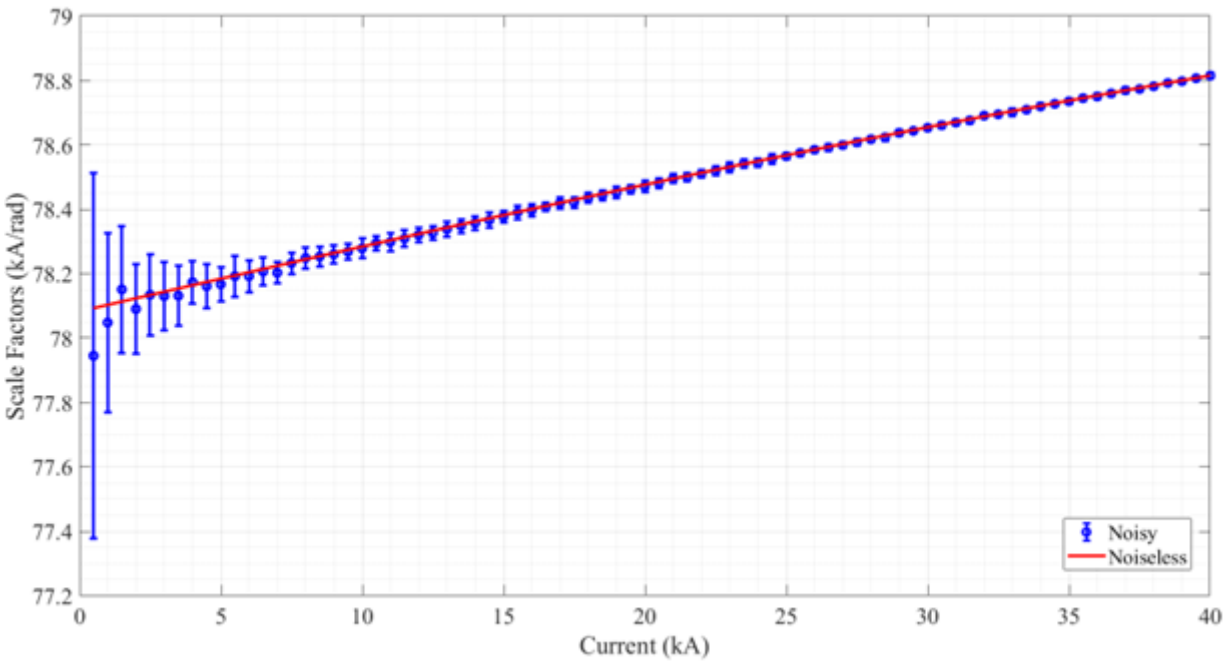

Figure 4.13. Error bar for the demodulated phase obtained by simulating each trace for 20 times with the detector noise. Red line represents the noiseless case.

Percentage error shown in Figure 4.14, agrees with the standard deviation of the scale factors in Figure 4.13. For currents smaller than 1 kA, noise heavily spoils the resulting phase. For currents above 3 kA, error decreases below 1%, and falls below 0.5% for currents higher than 15 kA.

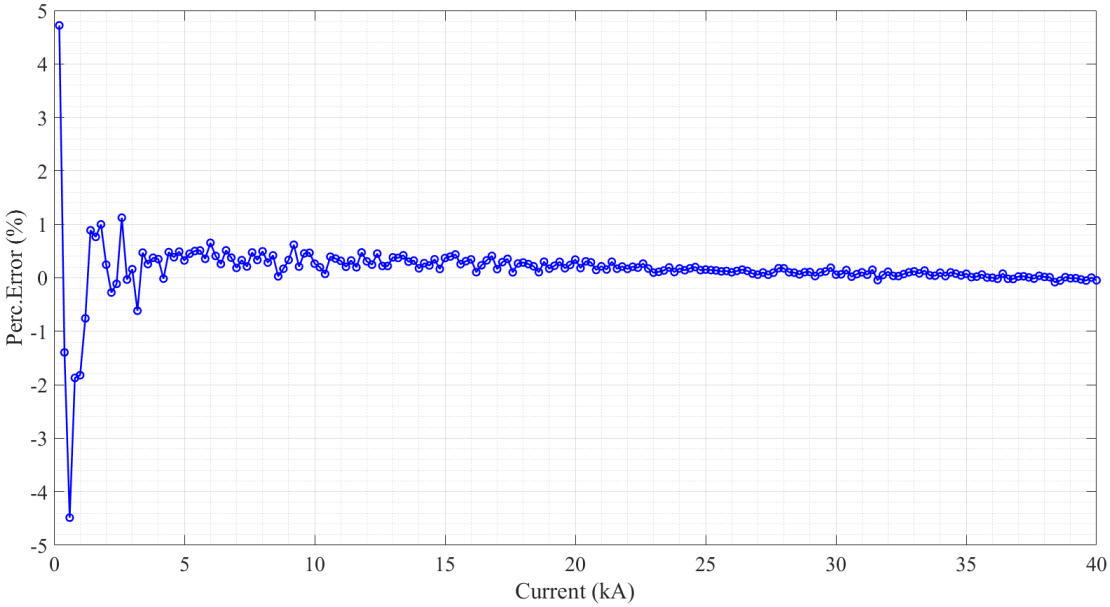

Figure 4.14. Percentage error obtained for currents from 200 A to 40 kA. All the mentioned effects are included.

CHAPTER 5

CONCLUSION

This study demonstrates that current measurement can be a new application area to Phase-OTDR technology. However, this area demands high accuracy which is met by two FBGs and a calibration process. The simulations show that, it can quantify currents from 1 kA to 40 kA with a percentage error less than approximately 1%.

As a future work, detector-noise-induced poor performance while sensing the currents below 1 kA may be improved by deep learning methods, e.g., denoising auto-encoders, recursive neural networks, long short term memory, etc.

Another projection is to multiplex our proposed sensor by interrogating successive sensing fibers coiled around different currents with multiplexed FBG pairs along a single fiber line, which can find applications in remote monitoring of different current sources,4 e.g., 3-phase systems in electrical grids or power stations. Also, the design can be converted to a quasi-distributed system by inscribing an array of FBGs along the sensing fiber rather than a pair of FBGs at both ends.

REFERENCES

Aerssens, M., A. Gusarov, P. Moreau, P. Malard, V. Massaut, P. Mégret, and M. Wuilpart (2012). Development of a jones vector based model for the measurement of a plasma current in a thermonuclear fusion reactor with a potdr setup. *Optical Sensing and Detection II 8439*(May 2012), 84390D.

Alasia, D. and L. Thévenaz (2004). A novel all-fibre configuration for a flexible polarimetric current sensor. *Measurement Science and Technology 15*(8), 1525–1530.

Barlow, A. J., J. J. Ramskov-Hansen, and D. N. Payne (1981). Birefringence and polarization mode-dispersion in spun single-mode fibers. *Applied Optics 20*(17), 2962.

Beller, J. (1998). Otdrs and backscatter measurement. In D. Derickson (Ed.), *Fiber Optic Test and Measurement*, pp. 454. Pearson College Div.

Blake, J. N., P. Tantaswadi, and R. T. de Carvalho (1994, sep). In-line Sagnac interferometer for magnetic field sensing. In *Tenth International Conference on Optical Fibre Sensors*, Volume 2360, pp. 419.

Bohnert, K., H. Brändle, M. G. Brunzel, P. Gabus, and P. Guggenbach (2007). Highly accurate fiber-optic dc current sensor for the electrowinning industry. *IEEE Transactions on Industry Applications 43*(1), 180–187.

Bohnert, K., P. Gabus, J. Nehring, and H. Brändle (2002). Temperature and vibration insensitive fiber-optic current sensor. *Journal of Lightwave Technology 20*(2), 267–276.

Born, M. and E. Wolf (1999). *Principles of Optics: Electromagnetic Theory of Propagation, Interference and Diffraction of Light* (7 ed.). Cambridge: Cambridge University Press.

Brown, M. (2017). Simulation of coherent phase optical time-domain reflectometry. Master's thesis, University of Manitoba.

Caucheteur, C., S. Bette, R. Garcia-Olcina, M. Wuilpart, S. Sales, H. Ottevaere, F. Berghmans, H. Thienpont, J. Capmany, and P. Mégret (2006). Use of the polarization properties of fiber bragg gratings for sensing purposes. *Optical Sensing II 6189*(April 2006), 618922.

Caucheteur, C., T. Guo, and J. Albert (2017). Polarization-assisted fiber bragg grating sensors: Tutorial and review. *Journal of Lightwave Technology 35*(16), 3311–3322.

Chen, Y., Y. Fu, J. Xiong, and Z. Wang (2021). Distributed Fiber Birefringence Measurement Using Pulse-Compression Φ-OTDR. *Photonic Sensors 11*(4), 402–410.

Cremonezi, A. O., E. C. Ferreira, A. J. B. Filho, and J. A. S. Dias (2013). A fiber bragg grating rms current transducer based on the magnetostriction effect using a terfenol-d toroidal-shaped modulator. *IEEE Sensors Journal 13*(2), 683–690.

Cubells-Beltran, M., C. Reig, J. Martos, J. Torres, and J. Soret (2011, 1). Limitations of magnetoresistive current sensors in industrial electronics applications. *INTERNATIONAL REVIEW OF ELECTRICAL ENGINEERING-IREE 6*, 423–429.

Dandu, P., A. Gusarov, P. Moreau, W. Leysen, S. Kim, P. Mégret, and M. Wuilpart (2022). Plasma current measurement in ITER with a polarization-OTDR: impact of fiber bending and twisting on the measurement accuracy. *Applied Optics 61*(9), 2406.

Donati, S., V. Annovazzi-Lodi, and T. Tambosso (1988). Magneto-optical fibre sensors for electrical industry: analysis of performances. *IEE proceedings. Part J, Optoelectronics 135*(5), 372–382.

Frosio, G. and R. Dändliker (1994). Reciprocal reflection interferometer for a fiber-optic Faraday current sensor. *Applied Optics 33*(25), 6111.

Gao, X. and B. Zhao (2019). A fiber optic current sensor on tunnel boring machine for current measurement application in tunnel geological prediction. *Optics and Lasers in Engineering 123*(July), 53–60.

Griffioen, W. and G. S. Glaesemann (2017). Optical fiber mechanical reliability. Technical Report July, Corning Inc.

Hartog, A. H. (2017). *An introduction to distributed optical fibre sensors*. CRC Press.

Huang, D., S. Srinivasan, and J. E. Bowers (2015). Compact tb doped fiber optic current sensor with high sensitivity. *Optics Express 23*(23), 29993.

Huang, Y., H. Chen, W. Dong, F. Pang, J. Wen, Z. Chen, and T. Wang (2016). Fabrication of europium-doped silica optical fiber with high verdet constant. *Opt. Express 24*(16), 18709–18717.

Jiao, B., Z. Wang, F. Liu, and W. Bi (2006). Interferometric fiber-optic current sensor with phase conjugate reflector. In *Proceedings of IEEE ICIA 2006 - 2006 IEEE International Conference on Information Acquisition*, pp. 707–711.

Jovicic, N. (2020). Reduction of polarisation effects in a phase-otdr using spun fibres. Master's thesis, Mons University.

Karabulut, D., A. Miazin, A. Gusarov, P. Moreau, W. Leysen, P. Mégret, and M. Wuilpart (2019). Effect of faraday mirror imperfections in a fiber optic current sensor dedicated to iter. *Fusion Engineering and Design 138*(October 2018), 48–52.

Kersey, A. D. and D. A. Jackson (1986). Current sensing utilizing heterodyne detection of the faraday effect in single-mode optical fiber. *Journal of Lightwave Technology 4*(6), 640–644.

Kocal, E. B. (2021). Development of simulation tool for fbg-based phase-otdr vibration sensors. Master's thesis, Izmir Institute of Technology.

Kumari, S. and S. Chakraborty (2018). Study of different magneto-optic materials for current sensing applications. *Journal of Sensors and Sensor Systems 7*(1), 421–431.

Laming, R. I. and D. N. Payne (1989). Electric current sensors employing spun highly birefringent optical fibers. *Journal of Lightwave Technology 7*(12), 2084–2094.

Leysen, W., A. Gusarov, P. Mégret, and M. Wuilpart (2019). Assessment of the environmental effects on the iter focs operating in reflective scheme with faraday mirror. *Fusion Engineering and Design 146*(December 2018), 805–808.

Li, C., J. Tang, Y. Jiang, C. Cheng, L. Cai, and M. Yang (2020). An Enhanced Distributed Acoustic Sensor with Large Temperature Tolerance Based on Ultra-Weak Fiber Bragg Grating Array. *IEEE Photonics Journal 12*(4), 1–11.

Liokumovich, L. B., N. A. Ushakov, O. I. Kotov, M. A. Bisyarin, and A. H. Hartog (2015). Fundamentals of Optical Fiber Sensing Schemes Based on Coherent Optical Time Domain Reflectometry: Signal Model under Static Fiber Conditions. *Journal of Lightwave Technology 33*(17), 3660–3671.

Lopez, J. D., A. Dante, T. Trovão, R. W. Mok, C. C. Carvalho, R. Celia, B. Allil, F. Borghi, and M. M. Werneck (2019). Optical Current Sensor Based on Magnetostrictive Composites. In *Proceedings of the Latin American Workshop on Optical Fiber Sensors 2019*, Number February 2020, pp. 87–90.

Masoudi, A., M. Belal, and T. P. Newson (2013). A distributed optical fibre dynamic strain sensor based on phase-otdr. *Measurement Science and Technology 24*(8), 85204.

Masoudi, A. and T. P. Newson (2014). Distributed optical fiber dynamic magnetic field sensor based on magnetostriction. *Applied Optics 53*(13), 2833.

Masoudi, A. and T. P. Newson (2017a). Analysis of distributed optical fibre acoustic sensors through numerical modelling. *Optics Express 25*(25), 32021.

Masoudi, A. and T. P. Newson (2017b). High spatial resolution distributed optical fiber dynamic strain sensor with enhanced frequency and strain resolution. *Optics Letters 42*(2), 290.

Motuz, R., E. Gescheidtova, W. Leysen, P. J. Moreau, A. Gusarov, P. Drexler, and M. Wuilpart (2019). Theoretical assessment of plasma current measurement in tokamaks in relation with the otdr detector noise. *Progress in Electromagnetics Research Symposium 2019-June*, 1511–1515.

Muanenda, Y., C. J. Oton, and F. Di Pasquale (2019). Application of raman and brillouin scattering phenomena in distributed optical fiber sensing. *Frontiers in Physics 7*, 155.

Nicati, P. A. and P. Robert (1988). Stabilised current sensor using sagnac interferometer. *Journal of Physics E: Scientific Instruments 21*(8), 791–796.

Ning, Y. N., Z. P. Wang, A. W. Palmer, K. T. Grattan, and D. A. Jackson (1995). Recent progress in optical current sensing techniques. *Review of Scientific Instruments 66*(5), 3097–3111.

Orr, P. and P. Niewczas (2011). Polarization-switching FBG interrogator for distributed point measurement of magnetic field strength and temperature. *IEEE Sensors Journal 11*(5), 1220–1226.

Papp, A. and H. Harms (1980). Magnetooptical current transformer 1: Principles. *Applied Optics 19*(22), 3729.

Peng, H., Y. Su, and Y. Li (2012). Evolution of polarization properties in circular birefringent fiber bragg gratings and application for magnetic field sensing. *Optical Fiber Technology 18*(4), 177–182.

Prakash, H. and N. Chandra (1971, 8). Density operator of unpolarized radiation. *Physical Review A 4*(2), 796–799.

Ramsden, E. (2006a). Chapter 1 - hall-effect physics. In *Hall-Effect Sensors: Theory*

and Application (Second Ed ed.)., pp. 1–10. Burlington: Newnes.

Ramsden, E. (2006b). Chapter 7 - current-sensing techniques. In *Hall-Effect Sensors: Theory and Application* (Second Ed ed.)., pp. 131–150. Burlington: Newnes.

Saleh, B. E. A. and M. C. Teich (1991, aug). Fiber Optics. In *Fundamentals of Photonics*, Wiley Online Books, pp. 272–309. John Wiley & Sons, Inc.

Saleh, B. E. A. and M. C. Teich (2007). Magneto-optics: The faraday effect. In *Fundamentals of Photonics* (2 ed.)., pp. 230–231. John Wiley & Sons, Inc.

Samimi, M. H., A. Mahari, M. A. Farahnakian, and H. Mohseni (2015). The rogowski coil principles and applications: A review. *IEEE Sensors Journal 15*(2), 651–658.

Satpathi, D., J. A. Moore, and M. G. Ennis (2005). Design of a terfenol-d based fiber-optic current transducer. *IEEE Sensors Journal 5*(5), 1057–1065.

Slatter, R., M. Brusius, and H. Knoll (2019). Magnetoresistive current sensors as an enabling technology for ultra-high power density electric drives. In *CIPS 2016 - 9th International Conference on Integrated Power Electronics Systems*, Number Figure 2, pp. 3–9.

Soto, M. A., X. Lu, H. F. Martins, M. Gonzalez-Herraez, and L. Thévenaz (2015). Distributed phase birefringence measurements based on polarization correlation in phase-sensitive optical time-domain reflectometers. *Optics Express 23*(19), 24923.

Tong, Y., Z. Li, J. Wang, H. Wang, and H. Yu (2018). High-Speed Mach-Zehnder-OTDR Distributed Optical Fiber Vibration Sensor Using Medium-Coherence Laser. *Photonic Sensors 8*(3), 203–212.

Vopálenský, M., P. Ripka, J. Kubik, and M. Tondra (2004). Improved gmr sensor biasing design. *Sensors and Actuators A: Physical 110*(1), 254–258.

White, A., G. McHale, D. Goerz, and R. Speer (2010, 10). Faraday rotation data analysis

with least-squares elliptical fitting. *The Review of scientific instruments 81*, 103108.

Wojcik, A. K. (2006). *Signal statistics of phase dependent optical time domain reflectometry*. Ph. D. thesis, Texas A&M University.

Woolsey, G. A., N. E. Fisher, and D. A. Jackson (1997). Tuning a bulk-glass optical current sensor by controlling conditions external to its reflecting surfaces. *Sensors and Actuators A: Physical 63*(1), 27–32.

Wu, B., F. Wen, K. Qiu, R. Han, and X. Lu (2013). Magnetically-induced circular-polarization-dependent loss of magneto-optic fiber bragg gratings with linear birefringence. *Optical Fiber Technology 19*(3), 219–222.

Wuilpart, M., M. Aerssens, A. Gusarov, P. Moreau, and P. Mégret (2017). Plasma current measurement in thermonuclear fusion reactors using a photon-counting potdr. *IEEE PHOTONICS TECHNOLOGY LETTERS 29*(6), 547–550.

Wuilpart, M., C. Caucheteur, A. Goussarov, M. Aerssens, V. Massaut, and P. Megret (2011). Measurement of magnetic field using Rayleigh backscattering in optical fibres. In *2011 2nd International Conference on Advancements in Nuclear Instrumentation, Measurement Methods and their Applications*, pp. 1–6.

Wuilpart, M., W. Leysen, A. Gusarov, P. Moreau, and P. Mégret (2018). Measurement of plasma current in tokamaks using an optical fibre reflectometry technique. *EPJ Web of Conferences 170*, 2017–2019.

Wuilpart, M., A. J. Rogers, P. Megret, and M. Blondel (2000). Fully distributed polarization properties of an optical fiber using the backscattering technique. *Applications of Photonic Technology 4 4087*(December 2000), 396.

Zhang, J., P. Li, Y. Wen, W. He, A. Yang, C. Lu, J. Qiu, J. Wen, J. Yang, Y. Zhu, and M. Yu (2012). High-resolution current sensor utilizing nanocrystalline alloy and magnetoelectric laminate composite. *Review of Scientific Instruments 83*(11), 1–6.

Zhang, Z., T. Guo, X. Zhang, J. Xu, W. Xie, M. Nie, Q. Wu, B.-O. Guan, and J. Albert (2016, 3). Plasmonic fiber-optic vector magnetometer. *Applied Physics Letters 108*(10), 101105. doi: 10.1063/1.4943623.

Zheng, J., X. Dong, P. Zu, J. Ji, H. Su, and P. Ping Shum (2013, 10). Intensity-modulated magnetic field sensor based on magnetic fluid and optical fiber gratings. *Applied Physics Letters 103*(18), 183511. doi: 10.1063/1.4828562.

Zhu, F., Y. Zhang, L. Xia, X. Wu, and X. Zhang (2015). Improved ϕ-otdr sensing system for high-precision dynamic strain measurement based on ultra-weak fiber bragg grating array. *Journal of Lightwave Technology 33*(23), 4775–4780.